Electrochemical Characterization of Iron Minerals

Miranda J. Bradley
B.S., Portland State University, 2011

A thesis presented to the faculty of
Environmental and Biomolecular Systems
at Oregon Health & Science University
in partial fulfilllment of the requirements for the degree
Master of Science
in
Environmental Science and Engineering

June 2020

The thesis “Electrochemical Characterization of Iron Minerals’ has been examined and approved by the following Examination Committee:

_____

Dr. Paul Tratnyek, Thesis Advisor

Professor, OHSU-PSU School of Public Health

_____

Dr. Tawnya D. Peterson, Committee Chair

Assistant Professor, OHSU-PSU School of Public Health

_____

Dr. Barbara Balko

Associate Professor of Chemistry, Lewis & Clark College

_____

Dr. Richard L. Johnson

Professor, OHSU-PSU School of Public Health

Acknowledgements

This research was supported by the National Science Foundation, award number 1333476. Samples of magnetite were donated by M. Scherer, C. Pearce, M. Villalobos. Data and materials for this project were collected in part by summer interns: Rachel Meeuwsen, Maria Fuentes-Deonate, Maya Navarro, Andrea Russel, Sarah Kwartler, and Zoe Luderman Miller. Advice on determining stoichiometry by acid dissolution provided over the years by Chris Gorski, Jim Szecsody, and Drew Latta. XRD data gathered by Kei Inoue and Anne K. Bentley of Lewis and Clark College. SEM-EDS data gathered by Greg Baty at Portland State University.

I am extremely grateful for the support I have received during my time at OHSU from the staff of the Student Health and Wellness center; it was integral to my success. I particularly want to recognize Dr. Lisa Schimmel, Dr. Carrie Milligan, Lindsay Field FNP, and Dr. Roger Batchelor as care providers I will have a very hard time replacing.

Thank you to my advisory committee for your guidance and advice as I entered the world of electrochemistry, particularly my advisor Dr. Paul Tratnyek for your patience and encouragement.

Finally, I am forever grateful for love and support of my partner Jennifer Sato. Thank you for enduring this challenging phase of our relationship with me, I do not take it for granted, and I look forward to making it up to you!

Table of Contents

List of Figures

List of Tables

List of Abbreviations

BET	Brunauer, Emmett and Teller (theory used to calculate SSA)
CP	chronopotentiometry
CPE	constant phase element
CRP	chemical reactivity probe
ECM	equivalent circuit model
EDS	energy dispersive x-ray spectroscopy
EIS	electrochemical impedance spectroscopy
iR	product of current and resistance
LPR	linear polarization resistance
LSV	linear sweep voltammetry
MRI	magnetic resonance imaging
mV	millivolt
nZVI	nano-zerovalent iron
PDE	packed disk electrode
RDE	rotating disk electrode
SEM	scanning electron microscope
SHE	standard hydrogen electrode
SSA	specific surface area
XRD	x-ray diffraction
ZVI	zerovalent iron

Abstract

The mixed and variable valence of iron in magnetite ($Fe(III)_{tet}[Fe(II),Fe(III)]_{oct}O_4^{2-}$) give this mineral unique properties that make it an important participant in redox reactions in environmental systems, but the variability in its stoichiometry and other physical properties complicates the determination of its effective redox potential. To address this challenge, a robust method was developed to prepare working electrodes with mineral powders of diverse characteristics and agarose-stabilized pore waters of controlled composition. This second-generation powder-disk electrode (PDEv2) methodology was used to characterize the electrochemical properties of magnetite samples from a wide variety of sources (lab-synthesized, commercial, and magnetically separated from environmental samples) using a sequence of complementary potentiometric methods: chronopotentiometry (CP), linear polarization resistance (LPR), electrochemical impedance spectroscopy (EIS), and then linear sweep voltammetry (LSV). The passive method CP gave open-circuit potentials (E_{OC}) and the active method LPR gave corrosion potentials ($E_{0,LPR}$) that agree closely with each other, but vary over a wide range for the magnetite samples tested (ca. 520 mV, from −267 to +253 mV vs SHE). The active method LSV gave values of $E_{0,LSV}$ that become increasingly more negative than E_{OC} for the samples with more positive potentials (by up to 189 mV). This effect is consistent with the cathodic polarization applied at the beginning of the LSV scan and suggests there is convergence of substoichiometric magnetites to the potential of stoichiometric magnetite after polarization. By all methods, lab-synthesized magnetites gave more negative potentials and smaller polarization resistances (R_p) than magnetite from commercial sources or magnetic-separation of environmental samples. This is consistent with the common notion that freshly synthesized minerals are more reactive, but clear correlations were not found between the measured redox potentials and surface area, iron stoichiometry, or magnetic susceptibility. All the measured potentials for magnetite fall in a range between calculated thermodynamic values for redox couples involving relevant iron species, which is consistent with the measured values being mixed potentials. The wide range in effective redox potential of magnetite is likely to influence its role in biogeochemistry and contaminant fate.

Chapter 1: Background

While Fe(III) oxides are the most ubiquitous iron minerals in critical zone environments,[1, 2] mixed-valent iron oxides containing Fe(II) and Fe(III)—including magnetite and green rust—are of special interest.[3] Magnetite ($Fe^{II}Fe^{III}_2O_4$) is the most stable mixed-valent iron oxide, and it is abundant in ferrigenous rocks, soils, and sediments.[4] Magnetite also plays important roles in corrosion of ferrous metals (making up much of the passive film on metallic iron surfaces), magnetic storage/recording media,[5-7] biology (e.g., in magnetotaxis),[8] medicine as a contrast agent in MRI imaging[9] and in cationic liposomes for drug delivery,[10, 11] nanotechnology (e.g., for functionalization of carbon nanotubes),[12, 13] and catalysis (e.g., synthesis of ammonia in the Haber-Bosch process).[14, 15] In all of these contexts, magnetite is a characteristically stable phase, but it participates as a conductor and/or electron donor in a variety of environmentally important redox processes such as corrosion of iron,[16, 17] metabolism by iron bacteria,[18-20] and abiotic reduction of contaminants.[21-27]

Among common environmental minerals, magnetite has the smallest band gap,[28] the highest conductivity,[29] and the lowest reduction potential.[3, 4] The conductivity of magnetite stems from the mixed-valence of iron in the mineral, which has an inverse spinel structure with Fe^{3+} in the tetrahedral sites and Fe^{2+} and Fe^{3+} in the octahedral sites (cartoon depiction in **Figure 1**). However, Mossbauer spectroscopy has shown that electrons from Fe^{2+} and Fe^{3+} in the octahedral sites delocalize, giving each iron atom a net charge of +2.5.[30, 31] Stoichiometric magnetite has a Fe^{2+}/Fe^{3+} ratio (x) equal to 0.5, but magnetite from the environment is commonly substoichiometric ($x < 0.5$) because Fe^{2+} is oxidized by dissolved or atmospheric O_2 and microbial respiration.[32-34] Other elements can replace the Fe^{2+} or Fe^{3+} in the magnetite structure, including magnesium, zinc, and nickel.[29] Among these dopants, Ti^{IV} is the most common impurity in natural magnetite, where it preferentially replaces Fe^{3+}, which results in magnetite that is superstoichiometric ($x > 0.5$).[23, 35] These differences in magnetite stoichiometry are expected to influence its properties related to material electronic structure, including magnetic susceptibility, conductivity, and redox potential.[21] Determining the appropriate redox potential to describe magnetite in biogeochemical systems is complicated by its irregular particle size, shape, and composition (e.g., doping); surface modifications by adsorption and weathering; and direct and/or mediated intraparticle interactions.

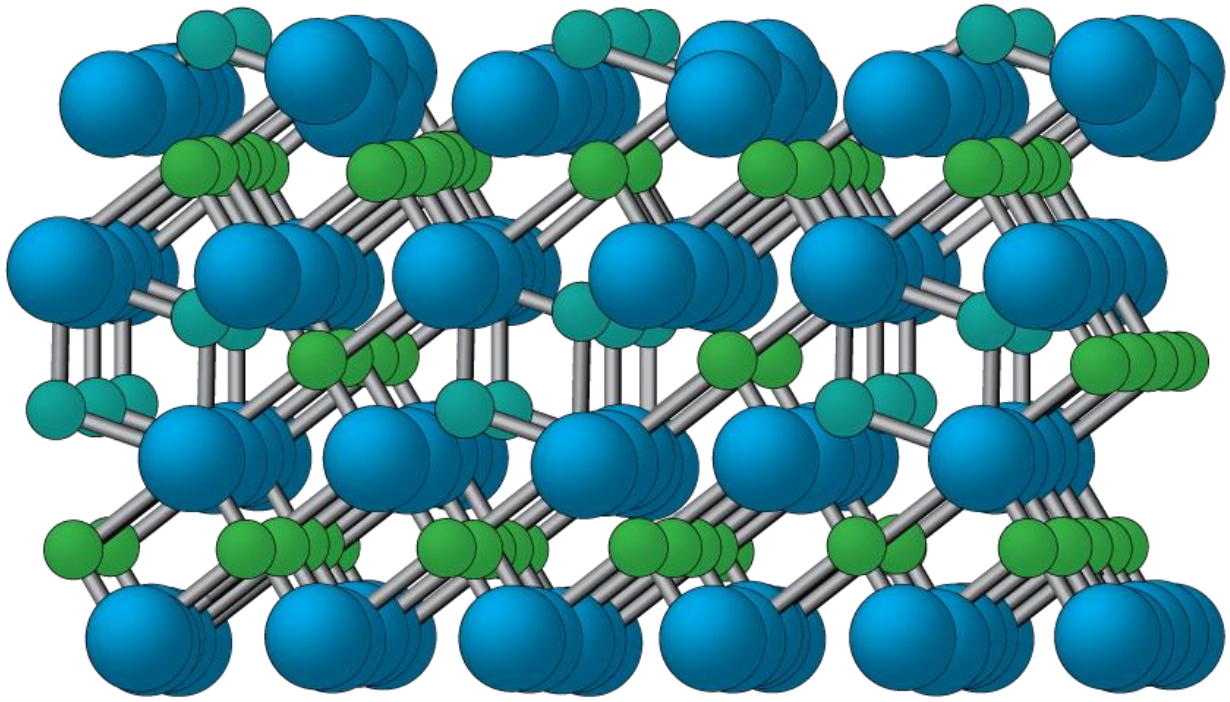

Figure 1. Cartoon representation of magnetite structure. Large blue spheres represent oxygen, teal spheres are in the tetrahedral position and are all Fe^{3+}, bright green spheres are in the octahedral position and are a combination of Fe^{2+} and Fe^{3+} (1:1 in stoichiometric magnetite).

Theoretical redox potentials for pure mineral phases can be calculated from thermodynamics,[36, 37] but the effective redox potential of natural materials is affected by other factors and therefore must be measured.[38] The redox potential of mineral samples can be measured by indirect methods, such as chemical reactivity probes (CRPs) with spectrophotometric detection[39] and electron-transfer mediators with potentiometric detection[40] or directly by using working electrodes prepared from the mineral samples.[30, 34, 41, 42] Electrodes made from polished bulk natural magnetite have been used to study open circuit potential,[30, 34] polarization resistance, and dissolution rate,[30, 41, 43] oxidation/reduction products,[30] and the effect of applied potential and electrolyte composition on surface stoichiometry.[34] Electrodes made by depositing (mostly) magnetite passive layers directly onto iron or steel rods have been used to study the effects of redox activity and coating integrity on corrosion processes.[44, 45] Composite magnetite electrodes, made with mixtures of magnetite and a conductive binder like graphite paste or carbon black, have been used to study the electrodissolution of magnetite,[42, 43, 46] and the capacitive behavior of magnetite in aqueous electrolytes.[47]

Additional methods have been used to study the electrochemisty of particulate materials other than magnetite, ranging from thin films of fine particles spin-coated onto disk electrodes to porous beds of coarse particles packed into columns.[48-50] In order to characterize intact nano- to micro-sized zerovalent iron (ZVI)—without grinding, polishing, sintering, etc.—we developed a "powder disk electrode" (PDEv1) wherein ZVI samples could be dry-packed into a millimeter-sized cavity in a cap covering a conventional rotating disk electrode.[51, 52] Electrochemical methods have been used with PDEv1 to characterize many aspects of the reactivity of granular ZVI, including the effects of electrode design and operational factors,[51] solution chemistry on the passive film,[53], nano-scale effects,[52, 54] aging and stability of zerovalent iron nanoparticles (nZVI),[54, 55] sulfidation of nZVI,[56, 57] effect of organic coatings,[58] and deposition of nZVI as a surface coating.[59] A much more limited amount of work has been done using PDEv1 to characterize iron minerals, mostly for control experiments to compare with ZVI,[52, 59] and just one study included PDEv1 measurements to characterize the redox properties of granular magnetite.[21]

Despite the success of prior work using PDEv1, the method has several limitations, including: (*i*) the material must pack well enough to stay in the cavity by compression alone, which precludes studying coarse materials, and (*ii*) packing dry particles into the PDEv1 and then immersing them into electrolyte results in unknown and possibly variable amounts of the pore space becoming filled with fluid. While we have not found that these limitations significantly complicate the interpretation of results, filling the pore space with a stabilizing fluid of controlled composition should make the electrode performance more robust and open up additional experimental opportunities, such as studying coarse particles, effects of pore solution chemistry, in situ deposition of secondary phases, etc. For this study, a modified method (PDEv2) was developed that involves packing the electrode with a wet slurry of the sample particles in a fluid composed of aqueous electrolyte and a non-reactive polymer to cause gelation. Agarose was chosen as the stabilizing polymer, based—in part—on a previously published method for making and studying model soil aggregates.[60] The PDEv2 method, which is first described here, produces a stable electrode that is able to withstand rotation up to 2000 rpm, pore fluid chemistry controlled by the recipe used to prepare the agarose, and an easily retrievable "puck" for further characterization after the completion of electrochemical experiments (**Figure 2E**).

The unique features of PDEv2 should eventually allow electrochemical characterization of biogeochemical redox processes at mineral-water interfaces, including the adsorption of Fe^{2+}, precipitation of iron oxides (or sulfides), mediation of electron transfer by shuttle compounds, long-range electron transfer via interparticle interactions, etc. However, the results reported in this study are limited to initial characterization of PDEv2 response using a relatively stable iron oxide (magnetite), simple solution chemistry (borate buffer), and a range of common potentiometric and voltammetric electrochemical methods. The results are used to address two process-level objectives: (*i*) clarification of the relationship between various definitions of "effective redox potential" and their application to (suspended, porous, or packed) particulate materials, and (*ii*) the relationship between redox potential of minerals and their impurities, particle size, surface coatings, etc. With respect to (*i*), this work appears to be the first systematic comparison of direct electrochemical methods for measuring redox potentials of mineral (and other material) powders, and demonstrates the diagnostic value of comparing passive and active potential measurement methods. With respect to (*ii*), the wide range of magnetite samples characterized, bracketed with data on more reduced and oxidized iron-based materials (i.e., Fe^0 and Fe_2O_3, respectively), provides a unique perspective on the sources of variability in these measured values, which allows identification of significant differences (e.g., due to passivating surface coating formed in the environment) and indeterminant variability due to sample heterogeneity, etc. One of the most significant differences observed was between relatively fresh magnetite synthesized in the laboratory and relatively-aged magnetite either purchased as chemical reagents or magnetically separated from sediment. While these differences in electrode potential measurements should be indicative of the material's reactivity, it was not possible to resolve the measured mixed potentials into the contributions of specific interfacial redox reactions.

Chapter 2: Experimental Section

2.1 Electrochemical system

Experiments were performed in a three-electrode cell, using 100 mL of 0.1875 M borate buffer at pH 8.4 (mainly for consistency with our prior work using PDEv1 and ZVI). The cell was sparged with N_2 throughout the experiment, at a flow rate of approximately 0.5 L/min. The working electrode was based on a ChangeDisk electrode from Pine Research Instrumentation (Durham), with a customized steel and Teflon-lined disk cavity (**Figure 2A**), which was filled with sample as described below and further in the supporting information. The Ag/AgCl (4M KCl) reference electrode and Pt coil wire (approximate surface area 4.7 cm^2) counter electrode were also from Pine. A steel and aluminum foil Faraday cage was used to minimize electronic noise. (**Figure 2B**) Experiments were run and data collected/analyzed with an Autolab PGSTAT30 potentiostat from Metrohm, running Nova 1.10 software.

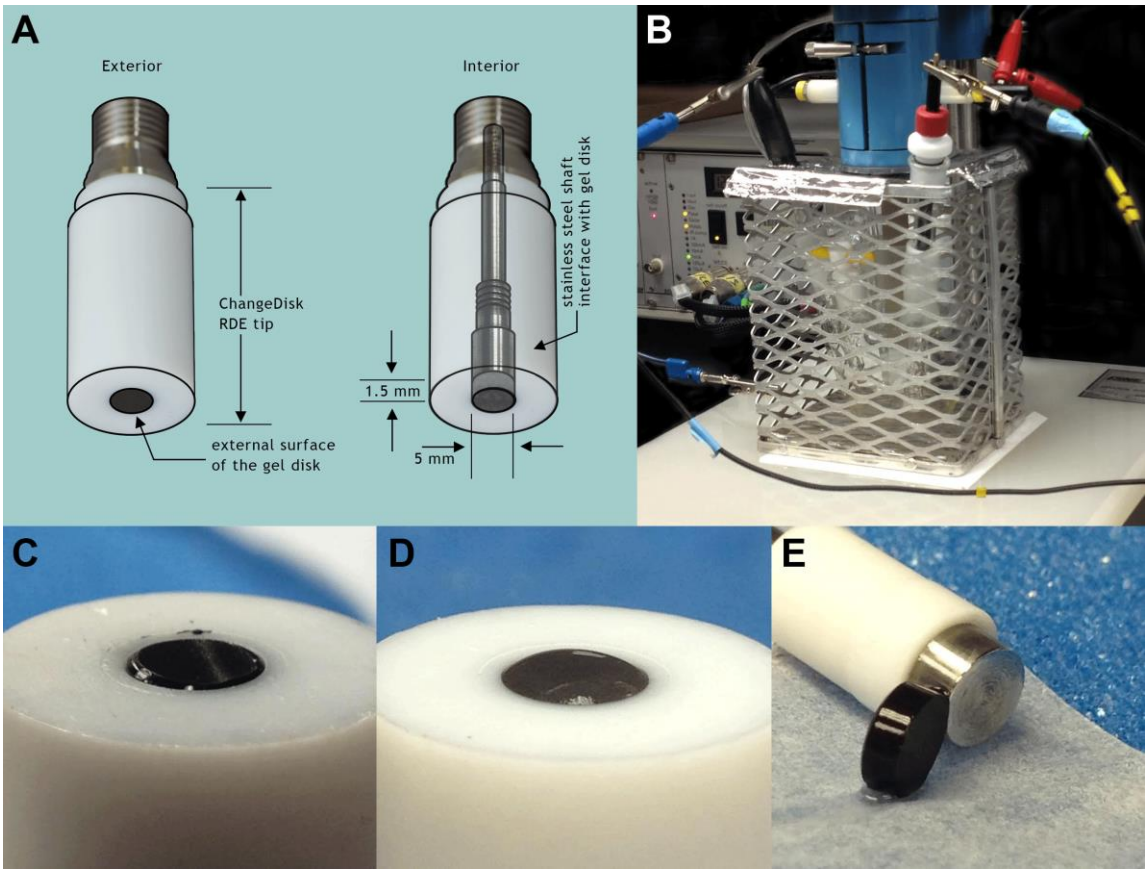

Figure 2. Configuration of the electrochemical cell used in this study. (A) Schematic of the PDE tip. (B) Photograph of the cell within the Faraday cage. (C) PDE surface, cut flat with a razor blade. (D) PDE surface left convex. (E) Recovered disk after experiment.

2.2 Custom working electrode

A variety of working electrode configurations and assembly protocols were investigated before settling on the method used in the study. Some of the preliminary results obtained during the development process are included in Appendix A. The powder disk electrodes (PDEs) were made by filling the cavity with the material of interest by suspending the sample in 1.5 to 2 wt% agarose gel (Fisher Agarose Low Melting, BP1360) made with the same buffer used in the cell. Agarose with a low melting temperature was used to avoid having to expose the samples to temperatures greater than 50ºC. The suspension was pipetted into the well of the ChangeDisk RDE tip (to slightly overfill the 30 μL cavity), and the tip was centrifuged for 15 minutes at 3200 rpm to ensure the sample was well-packed and had good connection to the steel shaft at the base of the well. After the primary centrifugation step, the surface was cleaned of debris and resurfaced with a thin layer of agarose gel to create a smooth, slightly convex interface with the electrolyte (**Figure 2D**).

2.3 Magnetite samples

A summary of all the magnetite samples used in this study—with standard materials properties and references to prior work with each material (when available)—is given in **Table 1** of Appendix B. Three commercially-sourced samples of magnetite were chosen as reference materials because they are readily available and have been characterized in prior studies: micron-sized magnetite powder from Bayferrox/Lanxess (Cologne) and nano and micron magnetite powders from Sigma-Aldrich (St. Louis). Several samples prepared with a (sub)stoichiometric ratio of Fe^{2+}/Fe^{3+} were obtained from M. Scherer's laboratory at the University of Iowa (Iowa City). Magnetite samples provided by C. Pearce (Pacific Northwest National Laboratory, Richland, WA) had been magnetically separated from sediment at the Hanford nuclear plant in Washington State, and samples from M. Villalobos lab (National Autonomous University of Mexico) had been isolated from iron ore deposits at the Pena Colorada mine in Mexico. Additional magnetically separated magnetite samples were obtained from a commercial supplier (Prospector's Choice, Surprise, AZ). We also magnetically separated magnetite from sediment samples collected from several locations in the Willamette river (Oregon) that had been dried

and size-fractioned. Maghemite (Fe_2O_3) from Alfa Aesar (Heysham), reference iron samples, and electrodes made with agarose alone were included for comparison.

2.4 Electrochemical experiments

The PDE was placed in the electrochemical cell containing 0.1875 M borate buffer (pH 8.4) as electrolyte and chronopotentiometry (CP, 0 A applied current) was performed by monitoring the open circuit potential (E_{OC}) while rotating the electrode at 2000 rpm. In early studies, CP was performed for 60 minutes and the E_{OC} at that time was recorded, but this period was extended to 14 hr (or more) in order to ensure that the electrodes had reached a consistent degree of equilibration. After CP, linear polarization resistance (LPR) was performed by measuring current (i) while applying a potential sweep—at a scan rate of 1 mV/s—from 10 mV below to 10 mV above the last recorded E_{OC}. LPR was repeated at least once, separated by 10-60 min of CP, to verify sample stability. After CP and LPR measurements, electrochemical impedance spectroscopy (EIS) was performed using a 10mV amplitude excitation signal over a range of frequencies from 10 kHz to 10 mHz. Finally, linear sweep voltammetry (LSV) was performed by applying potentials from 200 mV below to 200 mV above the last measured E_{OC}, at a scan rate of 1 mV/s. All potentials were measured versus Ag/AgCl reference electrodes, but are reported versus the standard hydrogen electrode (SHE). All polarization resistance (R_P) and corrosion current (i_{COR}) values were normalized to the geometric surface area of the exposed disk. More discussion on the use of surface area for normalization of data obtained with porous electrodes can be found in Appendix A.

2.5 Non-electrochemical characterization

To determine magnetite stoichiometry,[61-64] approximately 15 mg of sample was dissolved in 1 mL of HCl; commercial and collaborator-synthesized magnetite was dissolved in 5 M HCl, while magnetically separated samples required 12 M HCl for complete dissolution. The samples in acid were stored in an anaerobic glove box and were sampled by diluting 5 µL aliquots in 1 mL of 1 M HCl (Fe^{2+}) or 1 mL of 1.4 M hydroxylamine hydrochloride in DI water (Total Fe). The diluted samples were removed from the glovebox and further diluted into 1.5 mL cuvettes containing DI water, then 0.5 mM ferrozine in 0.5 M sodium acetate buffer was added. The ferrozine binds with the Fe^{2+} in solution to produce a magenta color with a maximum absorbance at 562 nm. Using a calibration curve, the total Fe and Fe^{2+} concentrations were determined and the Fe^{3+}

content of the original sample was calculated to determine the sample's Fe^{2+}:Fe^{3+} ratio. Sampling was done in triplicate with at least one replicate preparation.

To verify the commercial and magnetically separated samples were primarily magnetite, X-ray diffraction (XRD) analysis was performed using a Rigaku MiniFlex600 X-ray diffractometer with 40 kW/15 mA radiation (Willamette river samples used 40 kW/44 mA radiation). Diffraction patterns were collected over a range of 10 to 80º of 2Θ, using a step size of 0.04º and time per step of 0.5 s. The three samples that had not been previously characterized in other literature, magnetically separated magnetite from Prospector's Choice and two size fractions of magnetite from Willamette river sediment, were also characterized by scanning electron microscopy with energy dispersive X-ray detection (SEM-EDS) using a Zeiss Sigma VP FE-SEM.

Chapter 3: Results and Discussion

3.1 Chronopotentiometry (CP)

After each freshly-prepared PDE was first immersed into electrolyte, E_{OC} was recorded for up to 17 hours. Representative examples of this chronopotentiometric data (**Figure 3A)** show that E_{OC} became relatively stable (drift < 5 mV/hr) after about 3 hr of equilibration. E_{OC} was monitored until drift was < 2 mV/hr. No evidence for other changes—such as Flade potentials (also called passivation potentials) due to passive film breakdown[53]—were seen with any of the materials studied. Averages of the final values of E_{OC} across replicate measurements (subsamples of the same material in independently prepared PDEs) shows the expected overall trend of increasingly positive E_{OC} with magnetites that are less pure and/or more oxidized (**Figure 3B**). ZVI samples (presumably with a largely magnetite outer coating)[52, 54, 65, 66] had the lowest measured E_{OC}, while the laboratory synthesized magnetites that had been stored in an anaerobic chamber gave E_{OC} values that ranged from −267 mV for (nearly)stoichiometric magnetites to +159 mV for substoichiometric magnetites. Reagent grade magnetite that was purchased commercially (and not stored anaerobically) and magnetite that was magnetically separated from river sediments both gave measured values of E_{OC} that were similar to maghemite (**Figure 3A,B**).

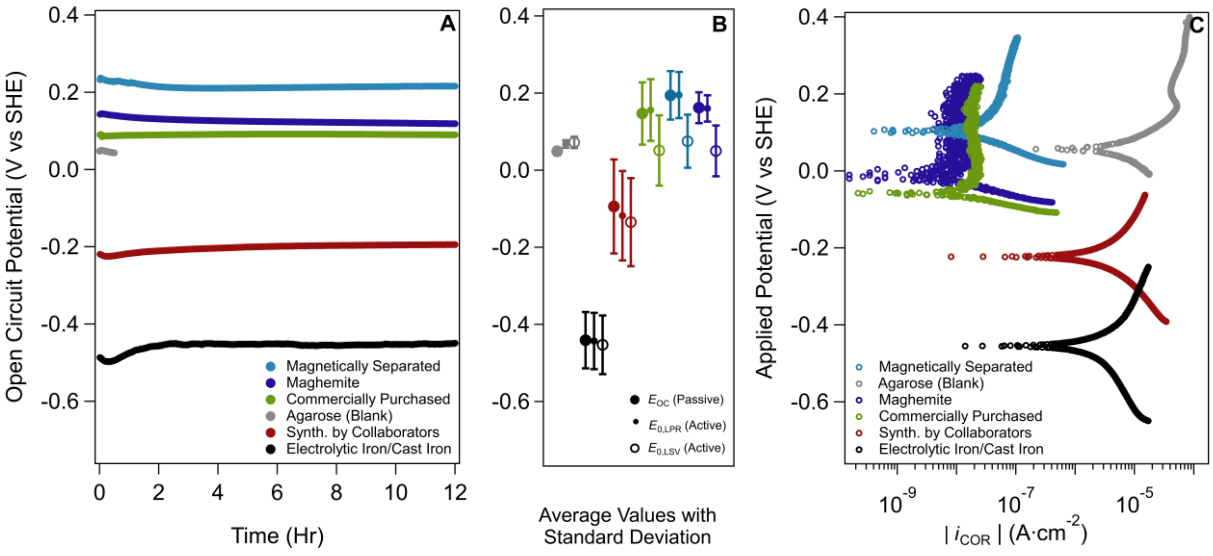

Figure 3. Representative potential measurements using PDEs: (A) E_{OC} by CP during the first 12 hr, (B) Average E_{OC} (passive), $E_{0,LPR}$ (active), and $E_{0,LSV}$ (active) values with standard deviations, and (C) Polarization by LSV at the end of each experiment shown in (A). Current in (C) was normalized to the geometric surface area of the exposed disk.

The error bars on the average values of E_{OC} (final) in **Figure 3B** reflect variability in all the data for each material type. The full set of data is summarized in **Figure 4A** (and tabulated in **Table 2** in Appendix B), where the x-axis represents the material sample used to prepare the PDE, with categories of material distinguished by color and ordered by expected degree of oxidation. For most materials, replicate measurements agree to within about 50 mV, which is similar to the consistancy obtained in prior work using single crystal magnetite electrodes.[30] In contrast, about one third of the samples included one or more final E_{OC} values that differ by up to 200 mV. This combination of generally consistent with occasional outlier measurements suggests one or more operational variables in the PDEv2 protocol are not well controlled. One possibility is inconsistency in the quantity of sample contained in the PDE cavity, but no relationship was seen between E_{OC} and the mass of sample material recovered from the PDE (**Figure 4B).** A second possibility is oxygen intrusion into the electrochemical cell, which is difficult to avoid completely even with continuous sparging with N_2.[59] While the PDE was prepared in an anaerobic chamber, electrochemical measurements were made on the benchtop and the sample material may have been exposed to varying amounts of oxygen during the transition. A third possible source of variability could be heterogeneity of the samples, both particle to particle and in the surface coating of the particles. To better understand the source and significance of the variability in E_{OC} measured passively by CP, these data are compared to potentials measured using the active methods introduced below.

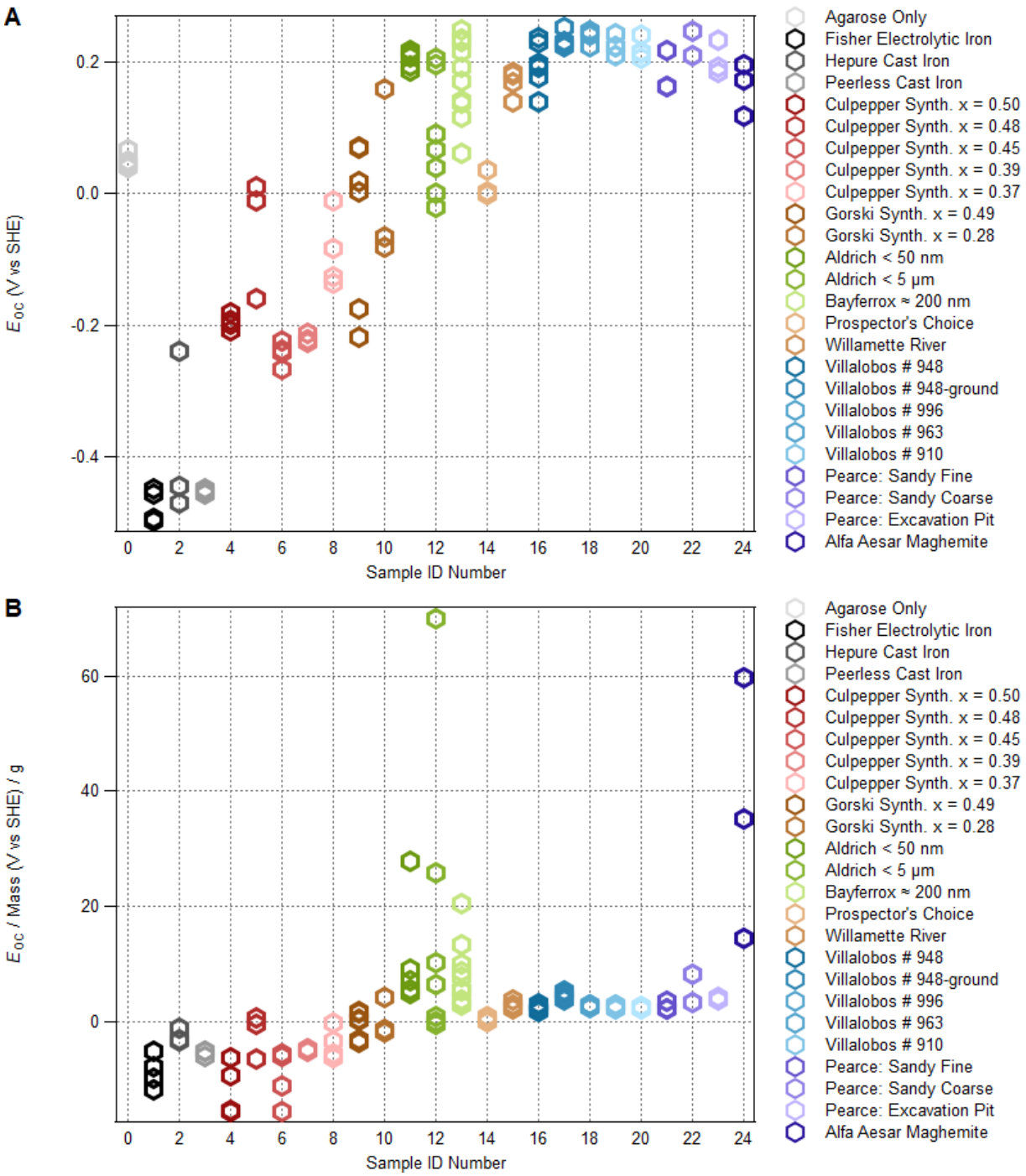

Figure 4. (A) Final E_{OC} measured by CP for each sample used in this study, showing the variability in redox potential over all samples. (B) Final E_{OC} measured by CP and divided by the mass of the recovered disk. Each marker represents a new electrode preparation. X-axis gives sample ID numbers that correlate with those listed in Tables 1, 2, 3, and 4 in Appendix B.

3.2 Linear Polarization Resistance (LPR)

After the passively measured E_{OC} was judged to be sufficiently stable (drift <2 mV/hr), the active but presumably nondestructive technique of LPR was performed by measuring current (i) while polarizing the electrode over a narrow potential range (±10 mV) relative to the last measured E_{OC}. Under these conditions, the response of current versus potential was linear and the data was fit by linear regression (example data and analysis is shown in **Figure 5**) to obtain the potential at $i = 0$ ($E_{0,LPR}$). **Figure 6A** shows that $E_{0,LPR}$ by the active method LPR agreed very well with E_{OC} obtained by the passive method CP. The strong correlation between E_{OC} and $E_{0,LPR}$ confirms that the potential applied during LPR did not significantly alter the samples, the individual methods contributed negligible indeterminant error, and there was no systematic bias between the two methods. The distribution of the different classes of samples along the correlation in **Figure 6A** demonstrates that the overall trend in potentials is ZVI < stoichiometric synthesized magnetite < substoichiometric synthesized magnetite < extensively aged or weathered magnetite/maghemite. However, within each class of materials there is considerable variability in potentials (ca. 200 mV) and across all the magnetite samples tested that range in potentials was quite large (~500 mV).

The slope obtained by regression on the current vs potential data from LPR was used to calculate the polarization resistance ($R_{P,LPR}$) of the electrode and sample. Plotting these data versus sample ID number (**Figure 7**) shows a pattern similar to that seen in the E_{OC} data (**Figure 4A**), and a (semi-log) plot of $R_{P,LPR}$ versus E_{OC} gives an overall correlation that appears to be significant (**Figure 6C**). However, this correlation is defined by clusters formed by the categories of materials, and does not seem to apply to the data within individual clusters. This result suggests that the main factor controlling R_P is bulk material type, which differs from the usual intepretation of R_P for a conventional electrode, where it reflects mainly the resistance to current flow across the electrode/electrolyte interface.[67] Before interpreting this result further, it is necessary to determine if R_P determined by LPR is as free of indeterminant error as the potential measurments. This is done in sections 3.3 and 3.4 by comparing $R_{P,LPR}$ to R_P determined by EIS and LSV.

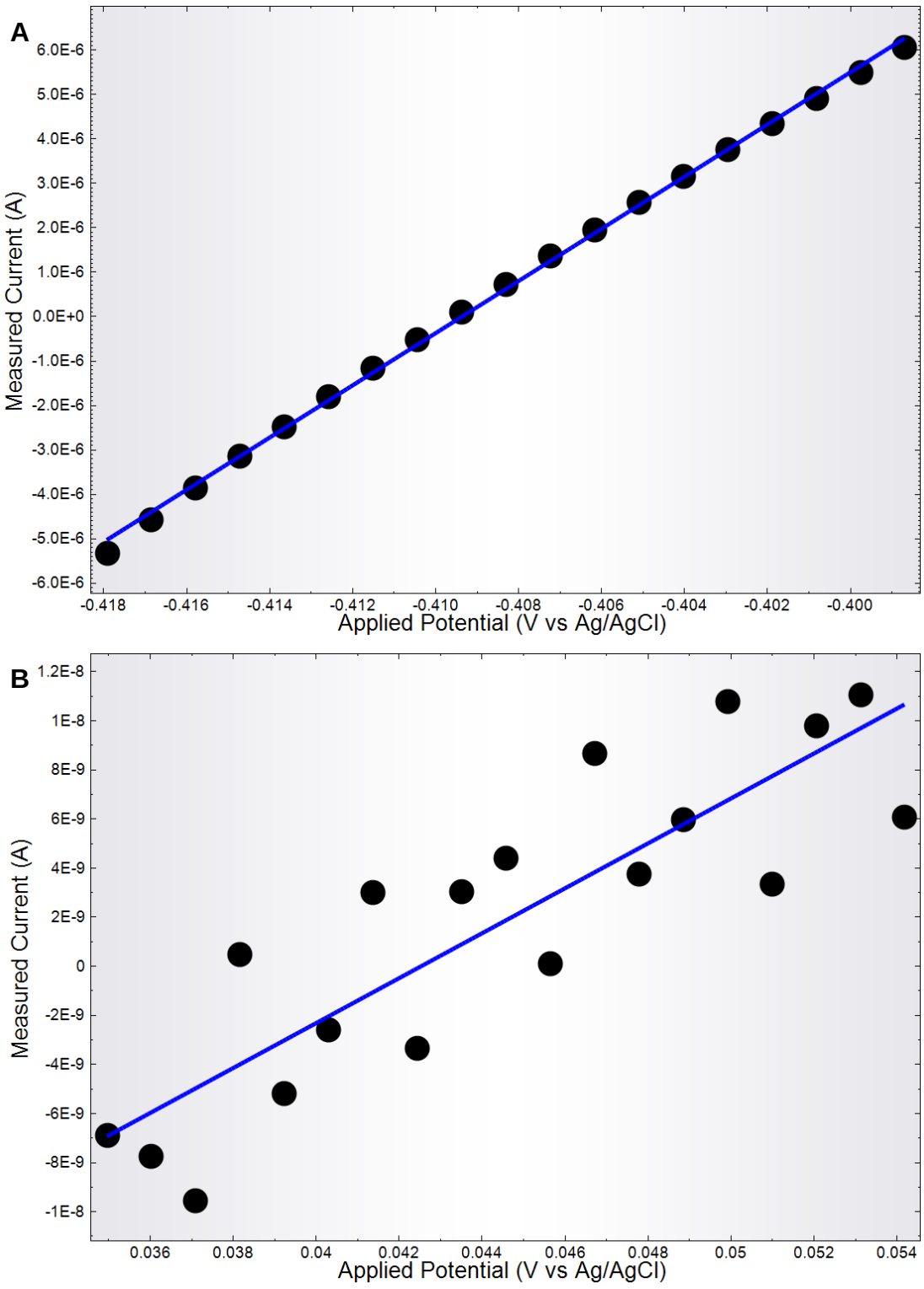

Figure 5. Example raw data with LPR analysis: (A) Magnetite synthesized by collaborators (x = 0.49), (B) Bayferrox magnetite.

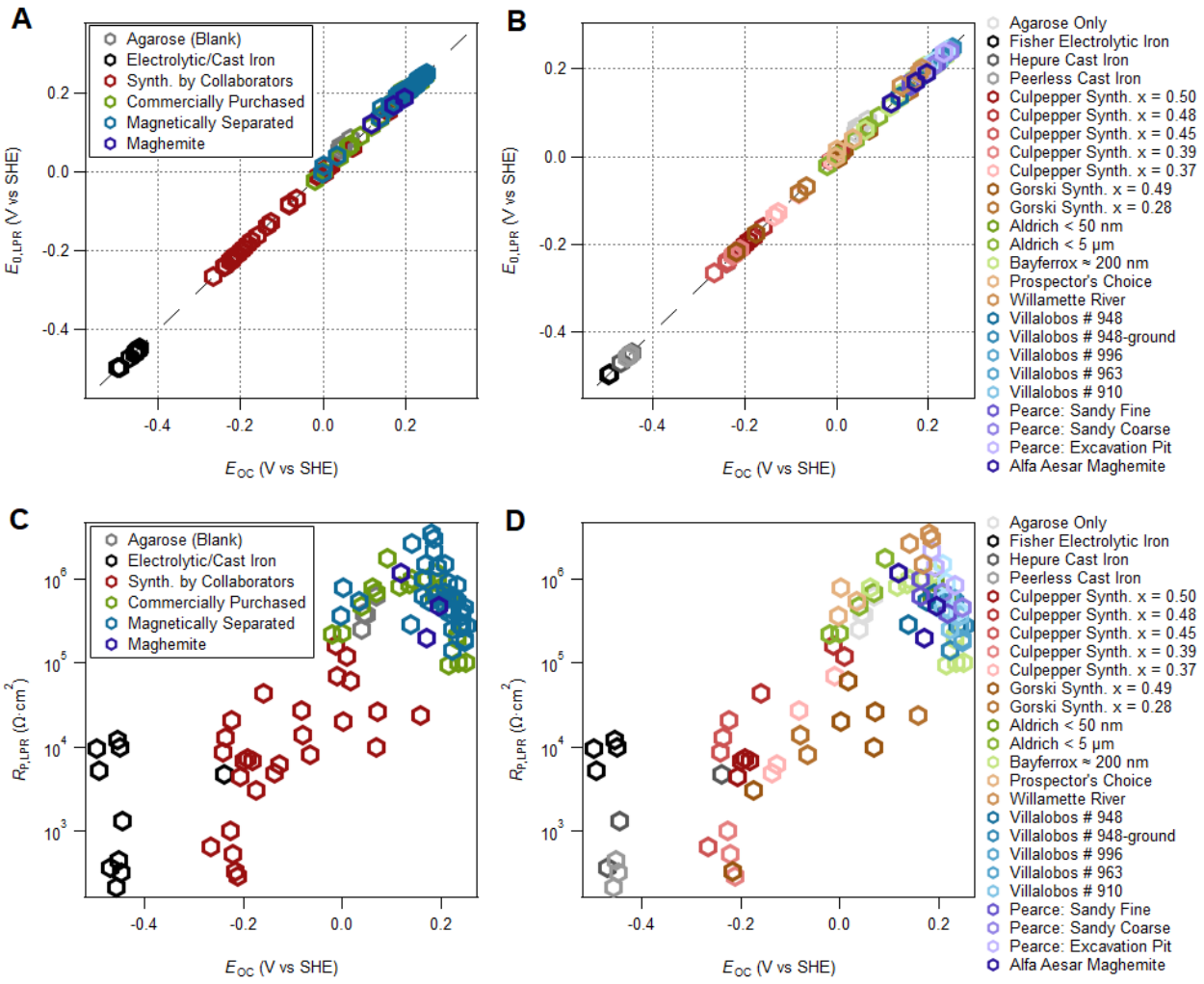

Figure 6. Comparison of redox potentials determined by different techniques and the relationship between redox potential and polarization resistance: (A) Active (y-axis) vs passive (x-axis) measurements of the redox potential, separated by sample type. (B) Polarization resistance ($R_{P,LPR}$) determined by LPR plotted against E_{OC}.

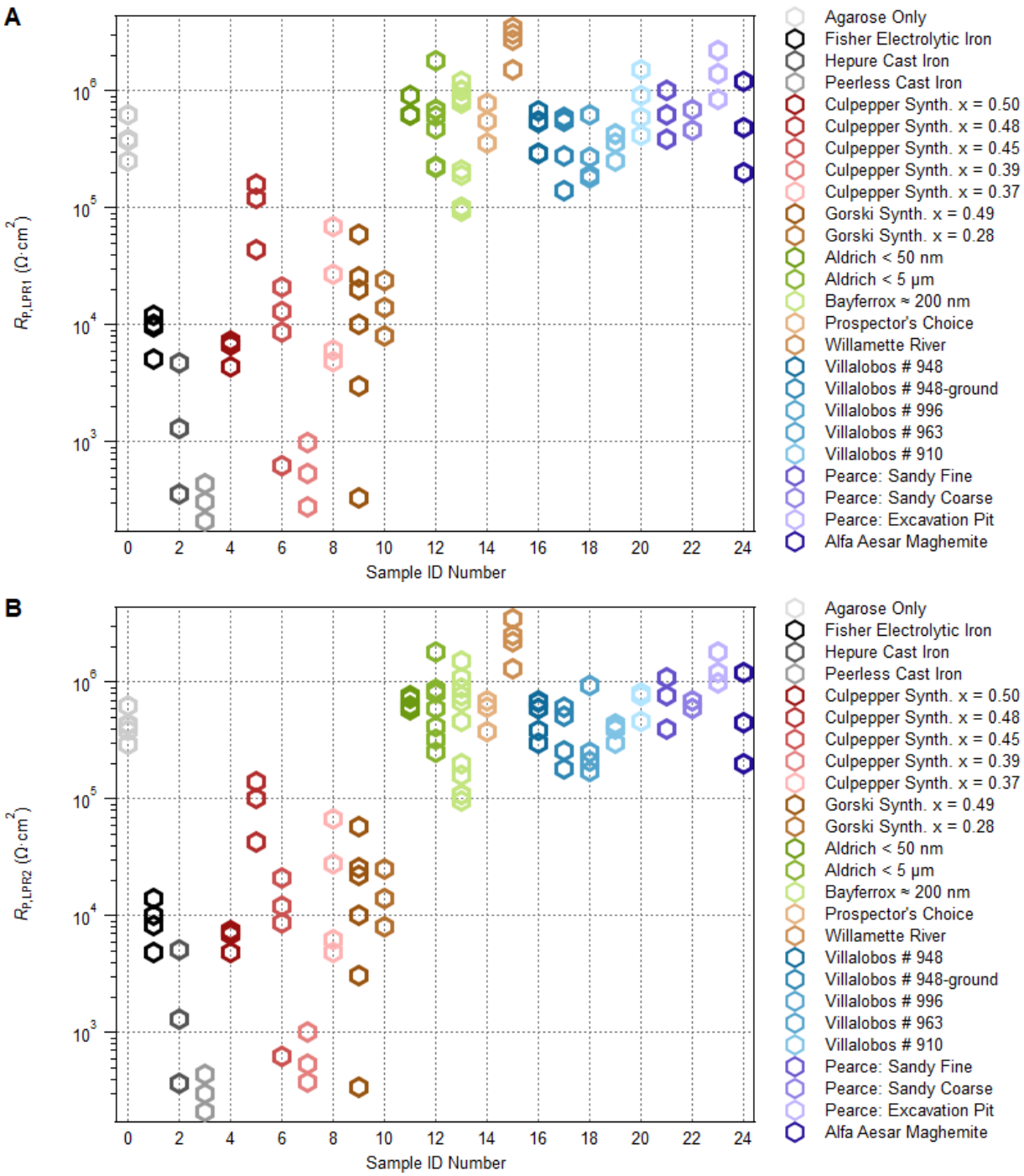

Figure 7. Polarization resistance ($R_{P,LPR}$) measured during first (A) and second (B) LPR for each sample used in this study, data normalized to the geometric surface area of the exposed disk. Each marker represents a new electrode preparation.

3.3 Electrochemical Impedance Spectroscopy (EIS)

As with LPR, EIS uses a perturbing signal of ±10 mV that is not expected to change the sample. This alternating potential was applied to the sample at varying frequencies (from 10 kHz to 10 mHz) and the resulting current signal was monitored to determine impedance (the ratio of potential to current) and phase shift (the lag of the current signal wave behind the applied potential wave). To aid in the analysis of the EIS data, an Equivalent Circuit Model (ECM) was selected. The ECM chosen for our cell configuration is shown in **Figure 8** and includes a resistor representing the resistance of the electrolyte and electrical connections of the potentiostat (RS), a resistor representing how easily charge can pass between the electrolyte and sample, or polarization resistance (R1), a Constant Phase Element (CPE) that represents the buildup of charge at the electrolyte/sample interface (CPE1), and a CPE representing the diffusion of charge through the sample (CPE2). CPE impedance is dependent on frequency, values reported here were calculated at 1 kHz. Examples of the raw data and ECM fit are shown in **Figure 9**, and analysis results are tabulated in **Table 4** of Appendix B.

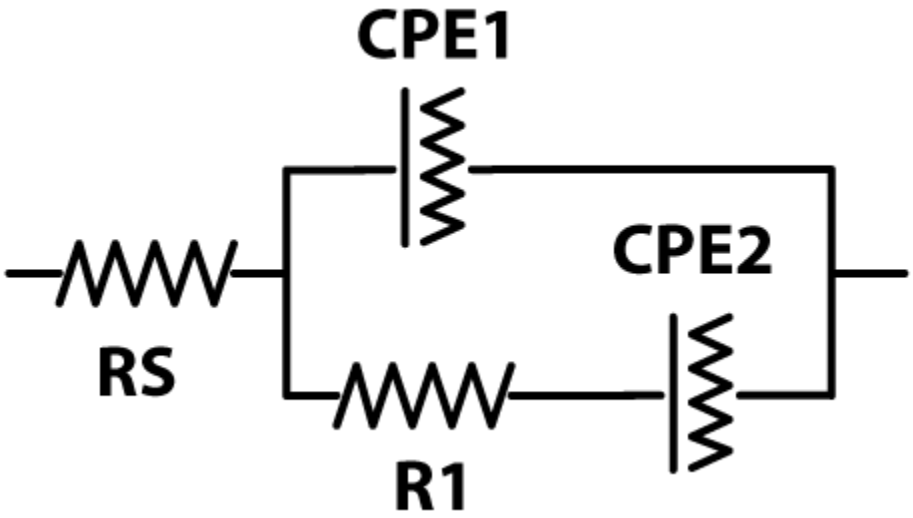

Figure 8. Equivalent Circuit Model chosen to analyze EIS data.

The resistance of the electrolyte and connections was not expected to vary significantly over time and between sample preparations, and was typically in the range of 300-500 Ω. The full set of data is summarized in **Figure 10A**, normalized to the geometric area of the electrode, and tabulated in **Table 4**. As seen in the figure, all preparations of the Willamette River sample had resistance values that were orders of magnitude greater than all other samples. It is not clear

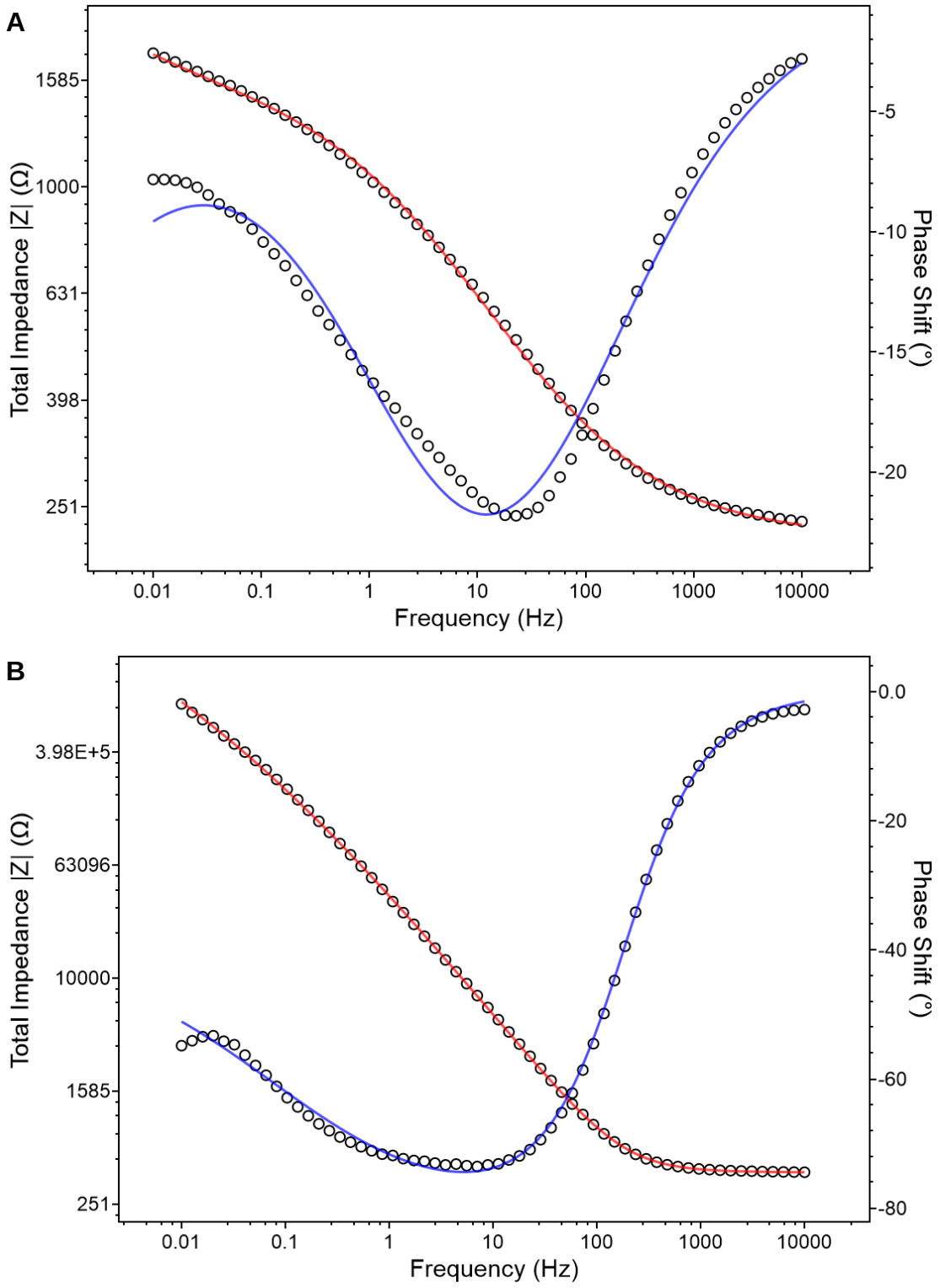

Figure 9. Example raw data showing ECM fit (red and blue lines) from EIS analysis: (A) Magnetite synthesized by collaborators (x = 0.49), (B) Bayferrox magnetite.

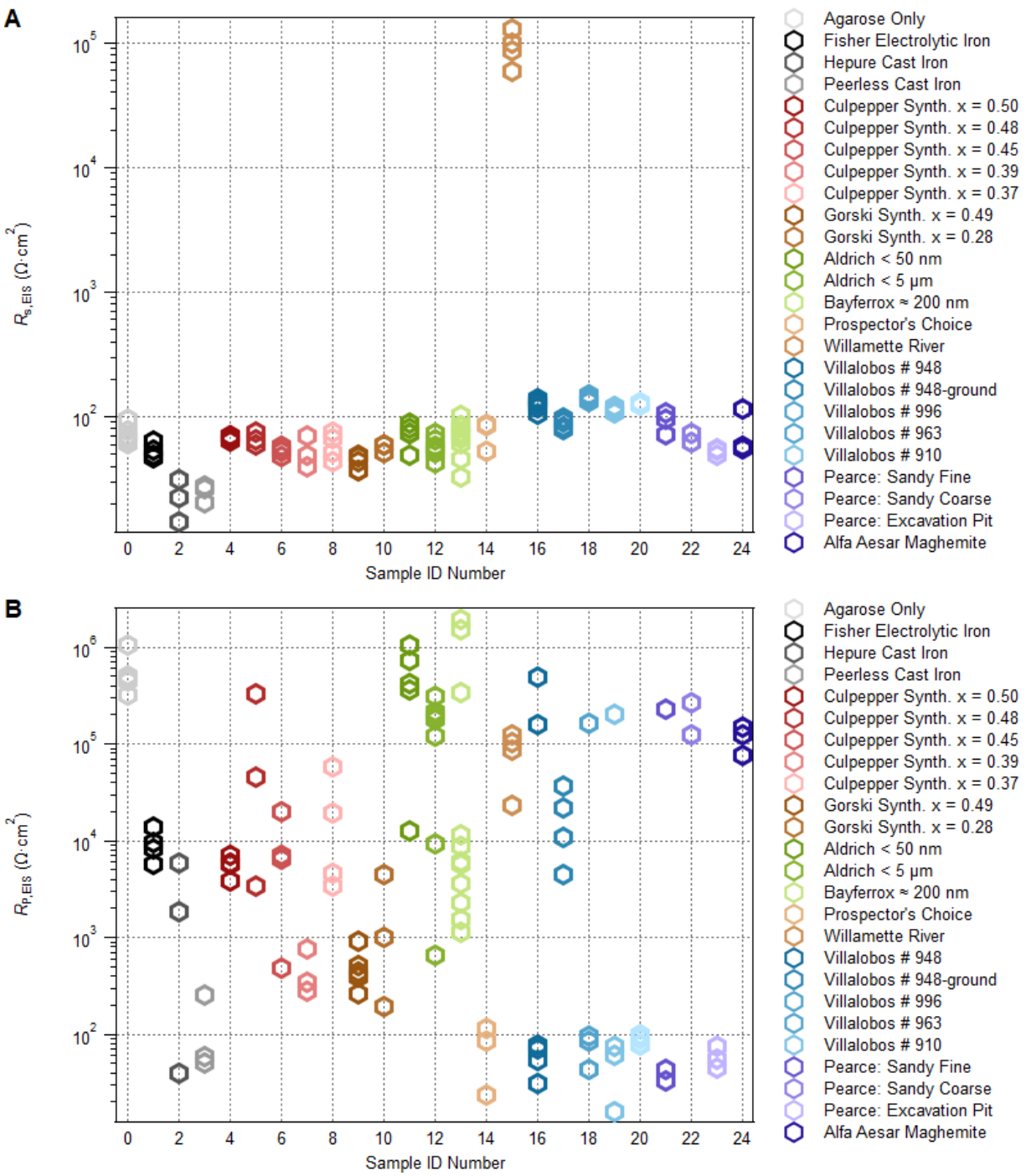

Figure 10. EIS/ECM determined values for (A) electrolyte resistance and (B) polarization resistance.

what caused this variation; possible causes include poor connectivity between the sample and the steel post at the base of the PDEv2 sample cavity, or a coating on the sample particles that is not accounted for in the ECM.

The polarization resistance determined by ECM analysis ($R_{P,EIS}$) was even more variable than that determined by LPR, and a significant portion of the magnetically separated samples had $R_{P,EIS}$ as low as some of the cast iron samples. **Figure 11** shows that around half of the sample preparations had good agreement between $R_{P,EIS}$ and $R_{P,EIS}$, a smaller portion was offset approximately an order of magnitude from the 1:1 line, and a cluster of the magnetically separated sample preparations were about 3 orders of magnitude lower. The pattern of iron samples < laboratory synthesized magnetite < commercial magnetite < magnetically separated magnetite seen in the CP and LPR data is absent in **Figure 11**.

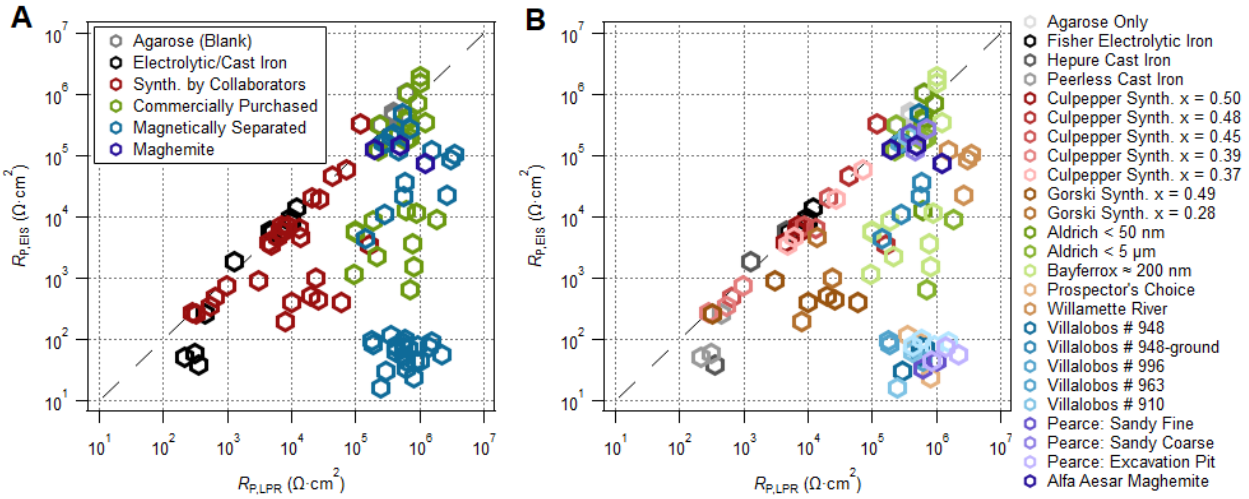

Figure 11. Polarization resistance determined by EIS and equivalent circuit analysis compared to polarization resistance determined by LPR, separated by (A) sample category and (B) specific sample.

The impedance values calculated for CPE1 and CPE2 are summarized for all samples in **Figure 12**. The outlier behavior of the Willamette River sample seen in the electrolyte resistance (**Figure 10A**) continues with the impedance of CPE1 in **Figure 12A**. On average, the laboratory-synthesized magnetite samples had the lowest CPE1 impedance, followed by the iron and commercial magnetite samples, and finally the magnetically-separated magnetite samples with the greatest impedance, on average. As CPE1 is thought to reflect the buildup of charge at the interface between the particles and the electrolyte, greater impedance could be an indication of a rougher surface that builds up more charge. However, plotting this value against the sample's

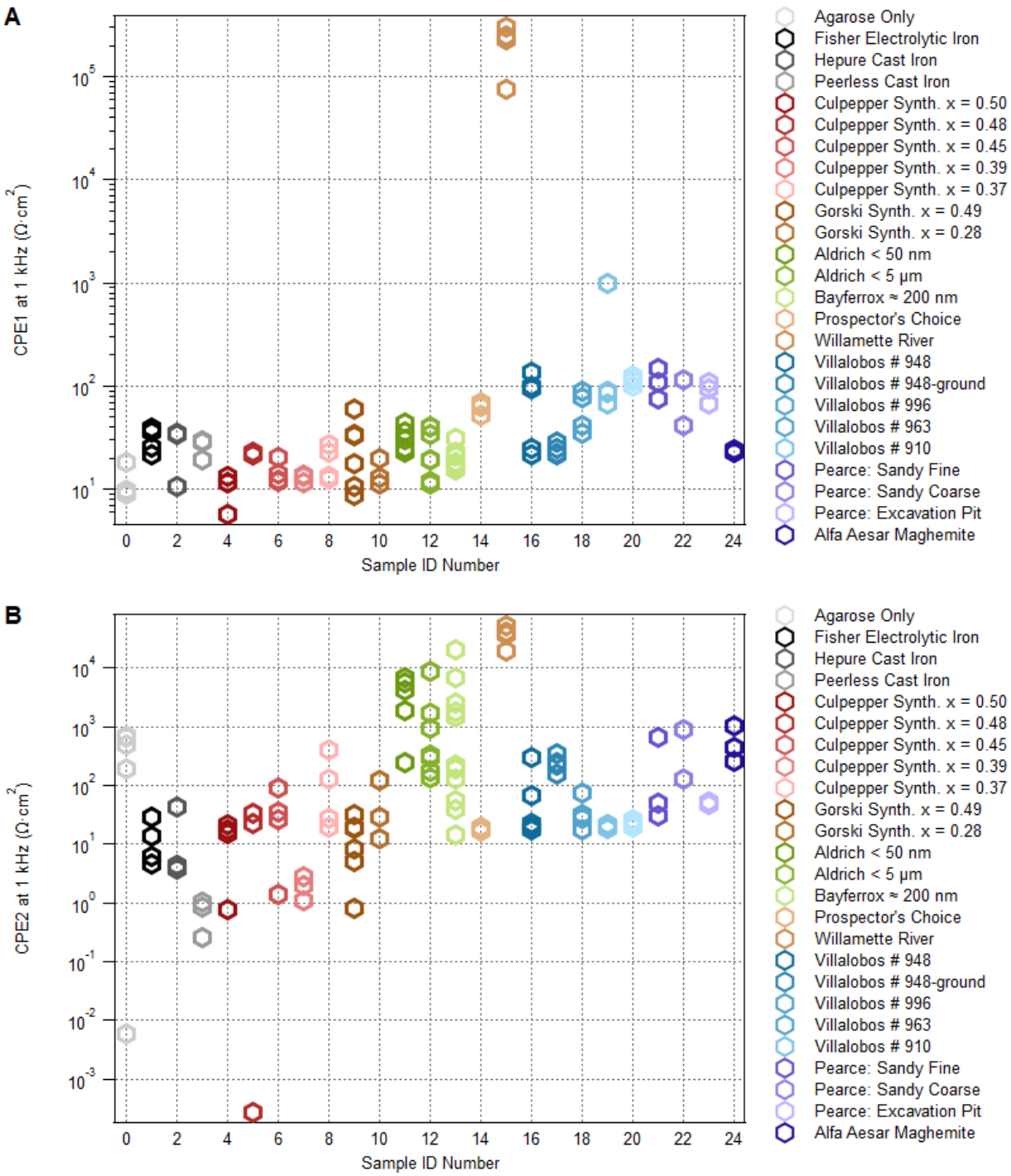

Figure 12. Constant Phase Element values calculated at 1 kHz, (A) CPE1 (B) CPE2.

total surface area (**Figure 13**) does not show a convincing correlation. Impedance of CPE2 (**Figure 12B**) was similar in magnitude to that of CPE1, with the Willamette River samples once again having the greatest impedance. Interestingly, the commercial magnetite samples also had greater CPE2 impedance on average than the other sample types. Further analysis of the CPE elements will be performed in the next section, as their impedance values are plotted against parameters determined by Linear Sweep Voltammetry.

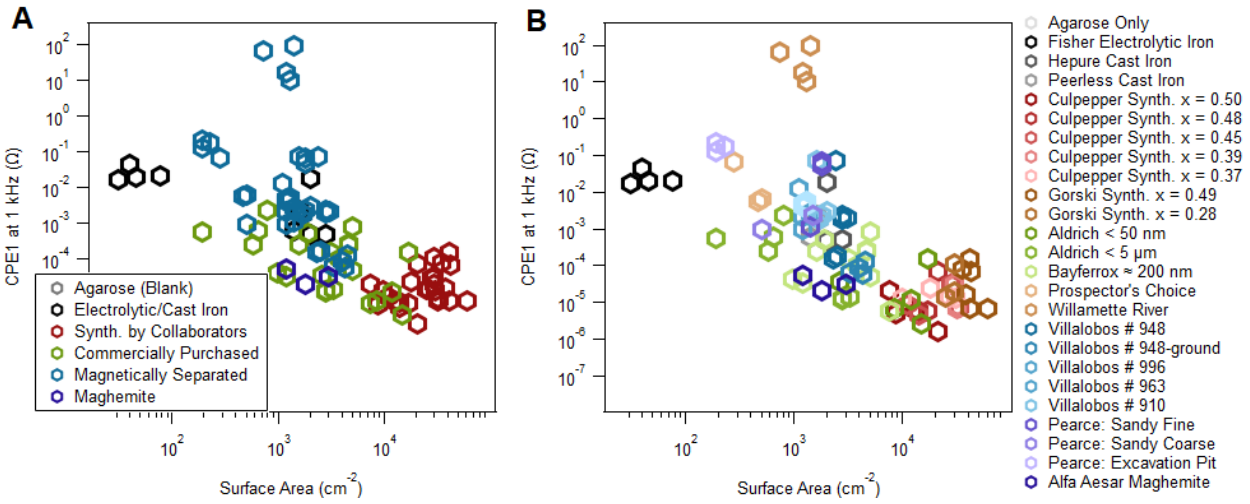

Figure 13. Impedance of CPE1 (before normalization by surface area) versus surface area (determined by multiplying the mass of the recovered dried sample disk by the sample's specific surface area, usually determined in lab by BET analysis), separated by (A) sample category and (B) specific sample.

3.4 Linear Sweep Voltammetry (LSV)

In contrast to LPR and EIS, the range of applied potentials used for LSV (from 200 mV below to 200 mV above the last measured E_{OC}) is large enough to significantly alter the sample, therefore it was applied at the end of the sequence of electrochemical methods used in this study. The LSVs shown in **Figure 3C** are representative of results obtained with the samples tested in this study and are typical of materials that exhibit reductive dissolution followed by oxidative passivation during cathodic to anodic polarization (including iron and iron oxides[52, 68]). The sharp peaks in **Figure 3C** occur at the potential where the net current switched from positive to negative ($E_{0,LSV}$), which should be equivalent to the potential represented by E_{OC} and $E_{0,LPR}$. However, careful comparison of the three types of potentials in **Figure 3** suggests that the values from LSV tend to be lower than those obtained by CP or LPR.

The relationship between $E_{0,LSV}$ (obtained from the LSV data where $i = 0$) and potentials determined by the non-destructive methods of CP and LPR is illustrated for E_{OC} in **Figure 14A**. In contrast to the strong 1:1 agreement between E_{OC} and $E_{0,LPR}$, the data for $E_{0,LSV}$ show a deviation that becomes increasingly negative as the potentials become more positive. This deviation is the expected result of cathodic polarization of the electrode during the initial portion of the LSV scan (which was started at −200 mV and held for 5 s, then scanned anodically at 1 mV/s), but the size of this effect and its relationship to other properties of the electrode materials is of interest. To explore this further, we calculated the difference in potential due to polarization ($\Delta E_{LSV/OC} = E_{0,LSV} - E_{OC}$) and plotted it vs. E_{OC} in **Figure 14C**. The overall trend in this figure shows that more oxidized magnetites are more susceptible to reduction, and additional experiments (not shown) confirmed that this effect becomes larger when polarization was performed at more negative potentials. The magnitude of ΔE probably reflects both bulk (e.g., stoichiometry) and surface characteristics (e.g., polarizability) of the material, both of which are discussed further below. Very similar results and identical conclusions would be obtained by comparing $E_{0,LSV}$ with $E_{0,LPR}$, instead of E_{OC}, so only the comparison to E_{OC} is shown.

The LSVs obtained on each sample were further analyzed by linear regression on i vs E at ±10 mV vs. $E_{0,LSV}$ (analogous to the method used on LPR data) and Tafel analysis (example raw data with Tafel slope fitting is shown in **Figure 15**). The linear regression method gave resistivity ($R_{P,R}$) from the slope, and these data are summarized in **Table 2** of Appendix B for all samples. Conventional Tafel analysis involves fitting the anodic and cathodic forms of the

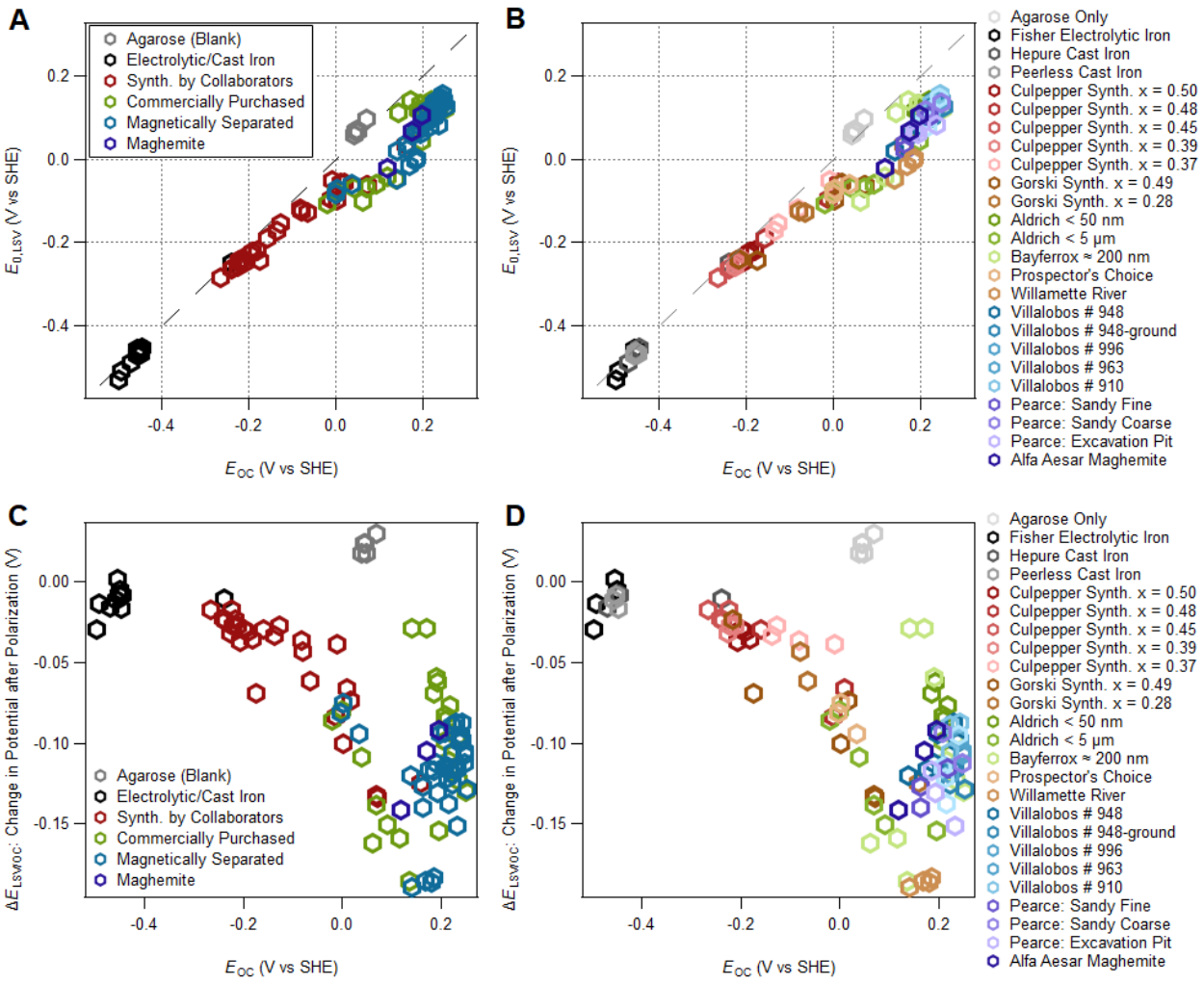

Figure 14. (A) Active (y-axis) vs passive (x-axis) measurements of the redox potential, separated by sample type. (C) The difference in potential ($E_{0,LSV}$ minus E_{OC}) vs E_{OC}.

Butler-Volmer equation to linear regions just below and above E_{OC} on log absolute current vs applied potential plots, [69-72] but many datasets do not show well-defined linear regions, so Tafel analysis is often criticized for being subjective. [73, 74] The data obtained in this study with PDEs were not well suited for Tafel analysis (e.g., **Figure 3C**, **Figure 15**), but application of additional criteria (e.g., that β_a and β_c should be less than 1 V/decade) resulted in a set of Tafel fits that seemed consistent within each LSV and across all the samples analyzed. The anodic and cathodic Tafel slopes (β_a and β_c), i_{COR} (**Figure 18A**) determined from the intersection of the two slopes at $E_{0,LSV}$, and **Equations 1 and 2** were used to calculate $R_{P,T}$.

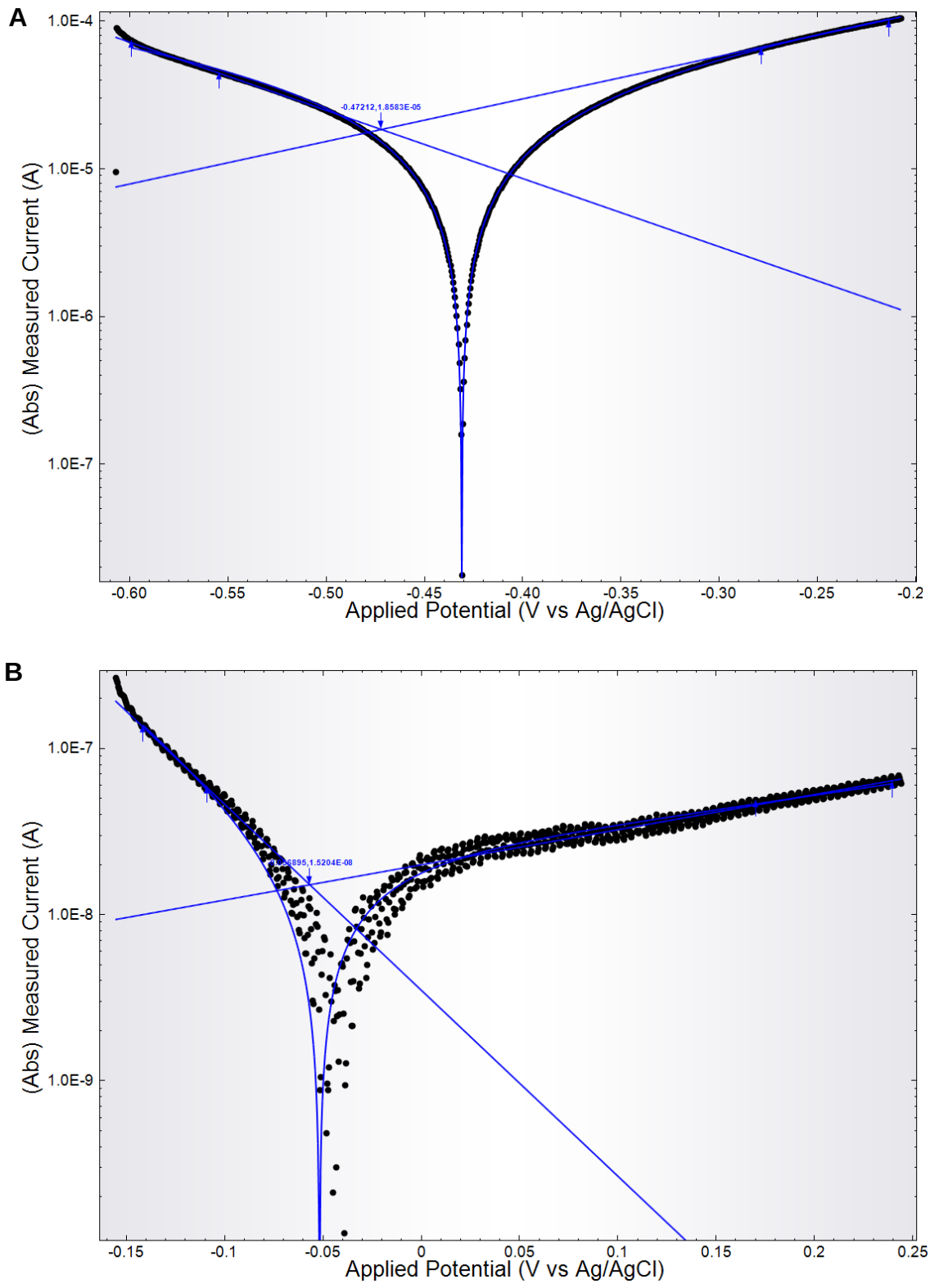

Figure 15. Example raw LSV data with Tafel analysis: (A) Magnetite synthesized by collaborators (x = 0.49), (B) Bayferrox magnetite.

$$\left(\frac{\Delta E}{\Delta I}\right) = R_{\mathrm{P,T}} = \frac{B}{i_{\mathrm{COR}}} \tag{1}$$

$$B = \frac{\beta_{\mathrm{a}}\beta_{\mathrm{c}}}{2.303(\beta_{\mathrm{a}}+\beta_{\mathrm{c}})} \tag{2}$$

The resulting values of $R_{\mathrm{P,T}}$ (**Figure 16A**, **Table 3)** are validated by the strong 1:1 correlation between $R_{\mathrm{P,T}}$ and $R_{\mathrm{P,R}}$, which is shown in **Figure 16A**.

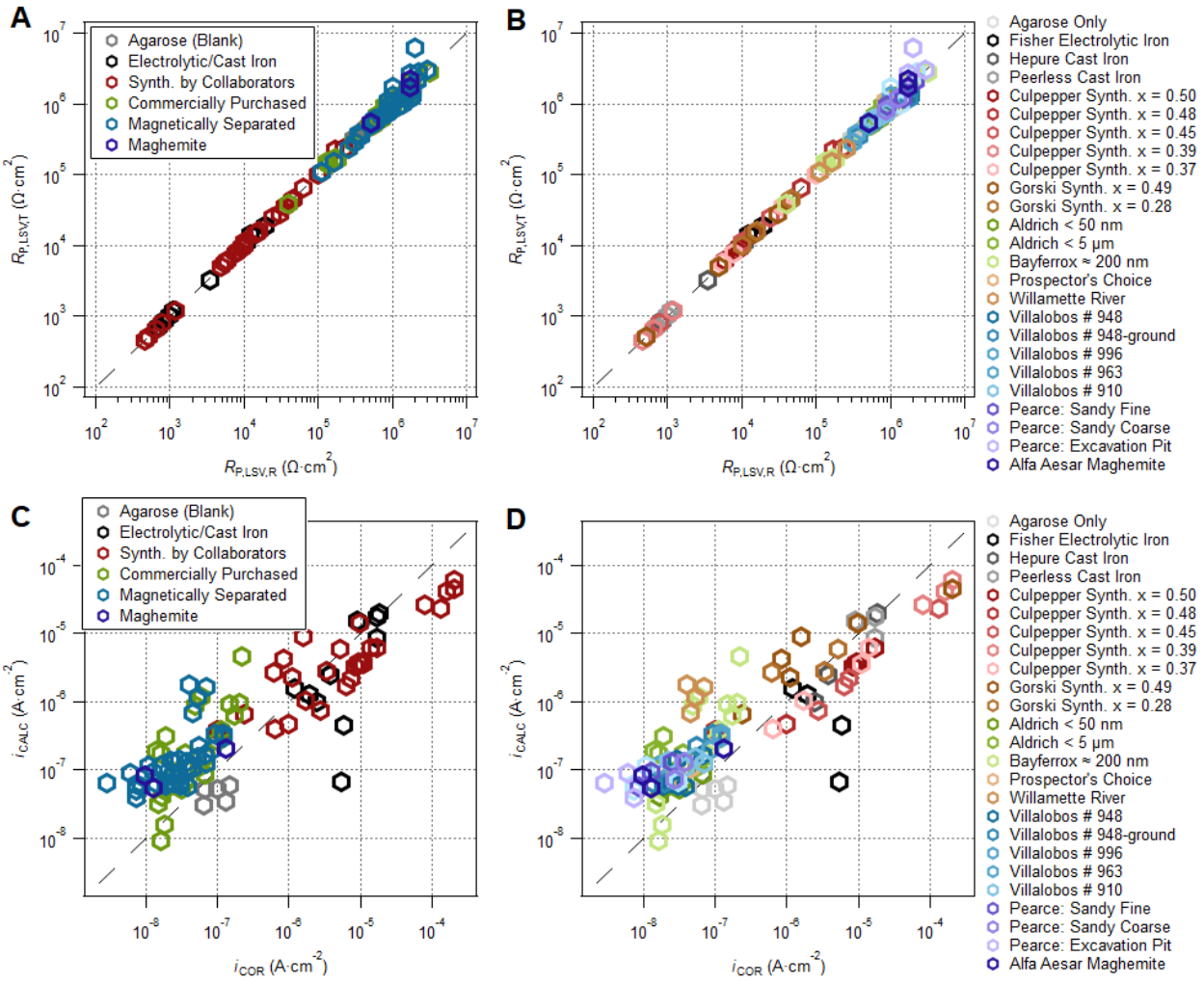

Figure 16. (A,B) Polarization resistance determined by Tafel analysis plotted against polarization resistance determined by the regression of the *i* vs *E* curve ±10 mV vs. $E_{0,\mathrm{LSV}}$. (C,D) Comparison of corrosion current calculated from the potential shift and polarization resistance to the corrosion current determined by Tafel analysis.

While Tafel slopes for simple corroding materials typically are in the range of 10's to 100's of mV/decade,[75] the values of β_{a} and β_{c} obtained in this study with magnetite PDEs ranged

from 14 up to 946 mV/decade (**Table 3** in Appendix B). Previous work that applied Tafel analysis to LSV data from electrodes made from freshly polished, bulk natural magnetite also noted a large range for anodic Tafel slopes (293-562 mV/decade), which the authors interpreted as evidence for transformation to oxidized surface phases.[30] Our previous work using packed powder disk electrodes (PDEv1) made of granular ZVI gave Tafel slopes in the range of 260-300 mV/decade, and we concluded that this range should be typical of porous and/or relatively resistive electrode materials.[56] The very wide overall range of Tafel slopes obtained in this study is consistent with the wide range of materials included in the scope as well as the non-ideal Tafel behavior of these materials, and non-ideal electrode characteristics of PDEs (compared with conventional polished disks).

The R_p values we calculated from the Tafel analysis agree well with the values determined by regression analysis (**Figure 16A**) and increase with the expected degree of oxidation, from an average $R_{P,T}$ of 8.1 kΩ·cm^2 for ZVI to 1.5 MΩ·cm^2 for maghemite (**Figure 18B**). As expected from eq 1, the associated i_{COR} values show the opposite trend, with an average i_{COR} of 38 nA·cm^{-2} for magnetically separated magnetite to 33 μA·cm^{-2} for collaborator-synthesized magnetite (**Figure 18A**). Inspection of **Figure 18** shows that there is roughly twice as much scatter in the data from the collaborator-synthesized magnetites as there is for the commercial or magnetically-separated magnetites. This pattern might reflect differences in the composition of the surface passivation layers of these two groups: (*i*) the commercial and magnetically separated magnetite samples likely were highly passivated due to extended exposure to atmospheric oxygen, and this would cause all the sample coatings to converge to the most stable composition; whereas (*ii*) the collaborator-synthesized magnetites should be minimally passivated because they were stored anaerobically and only briefly exposed to oxygen during transfer of the electrode from the glove box to the electrochemical cell, so small variations in exposure during this period might produce large differences in their less-well established passivation layers.

To compare with the corrosion current data we obtained from the Tafel analysis (i_{COR}), we also calculated corrosion current (i_{CALC}) with Ohm's law ($I = E/R$) using the observed shift in potential due to polarization ($\Delta E_{LSV/OC}$) and the resistance obtained from regression analysis of the LSV data ($R_{P,R}$). The resulting values of i_{CALC} are given in **Table 2** and the correlation

between i_{CALC} and i_{COR} is shown in **Figure 16C**. This correlation shows significant scatter and deviation from the 1:1 line, in contrast to the very tight 1:1 correlations between E (**Figure 6A**) and R_P (**Figure 16A**) obtained by complementary methods. If a significant portion of this scatter is indeterminant error, it must come from the difference in potential ($\Delta E_{LSV/OC}$) used to obtain i_{CALC}, because **Figure 16A** shows there is negligible uncertainty in $R_{P,T}$ and $R_{P,R}$. Instead, it is likely that the scatter and deviation from 1:1 slope in **Figure 16B** simply reflect the lack of a direct relationship between R_P and β.

One notable feature of **Figure 16** is the overlap between R_P and i_{COR} for synthesized magnetite vs. ZVI, which even results in some synthesized magnetites having lower R_P and higher i_{COR} than ZVI. This relationship contrasts with the potential measurements (**Figure 6A** and **Figure 14A**), which show a wide separation between the ZVI samples and the magnetite synthesized by collaborators. An implication of this unexpected result is that synthesized magnetite could be more reactive than ZVI with some solutes under some conditions (since R_P and i_{COR} are related to ease of interfacial electron transfer[76, 77]).

To further compare parameters determined by complementary methods, the CPE impedance determined by EIS is plotted against i_{COR} in **Figure 17**. Although the scale is skewed by the outlier data points, the expected trend of higher impedance correlating with lower current can be seen for both CPE1 and CPE2.

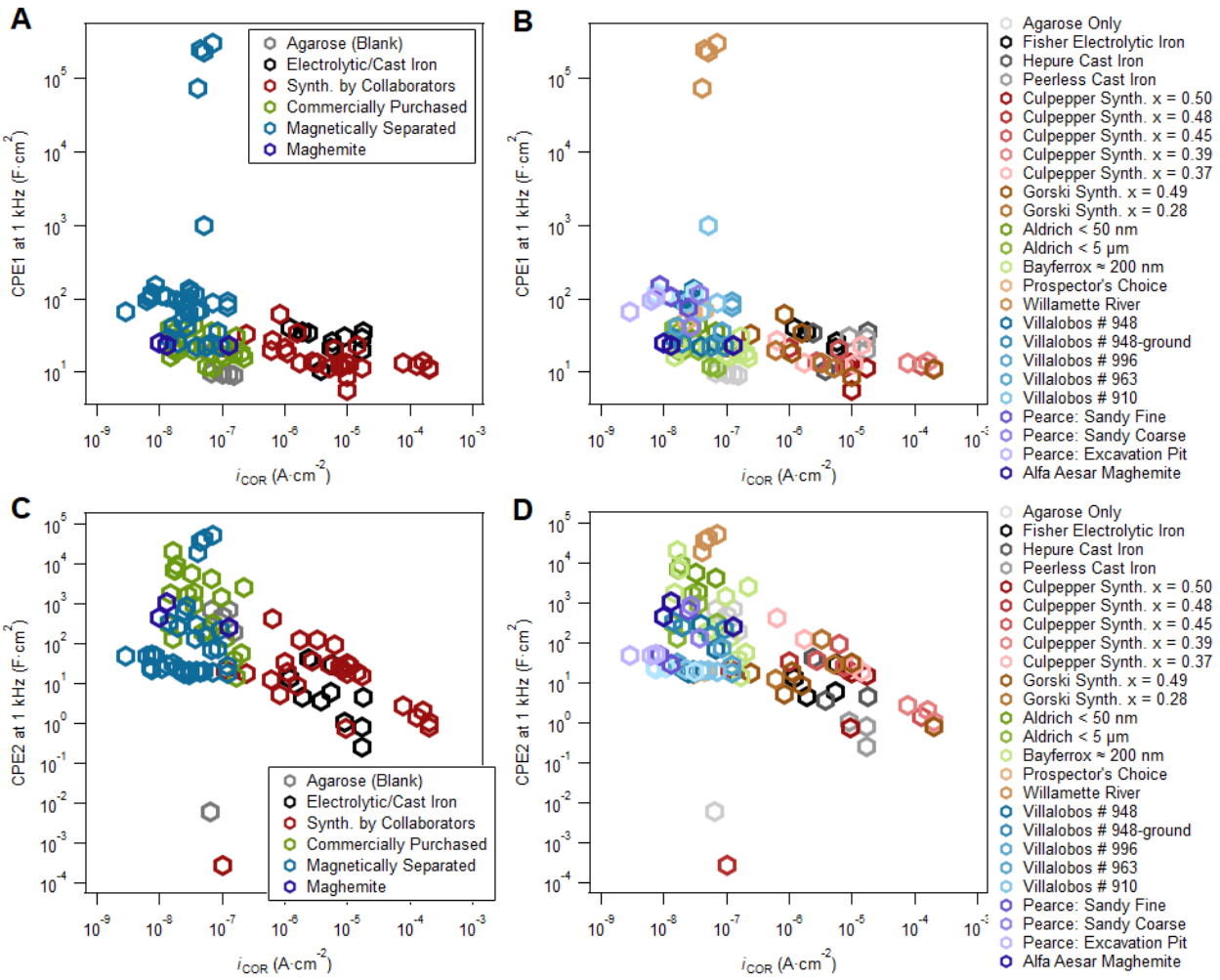

Figure 17. Constant phase element impedance values at 1 kHz compared to corrosion current. (A,B) CPE1, (C,D) CPE2.

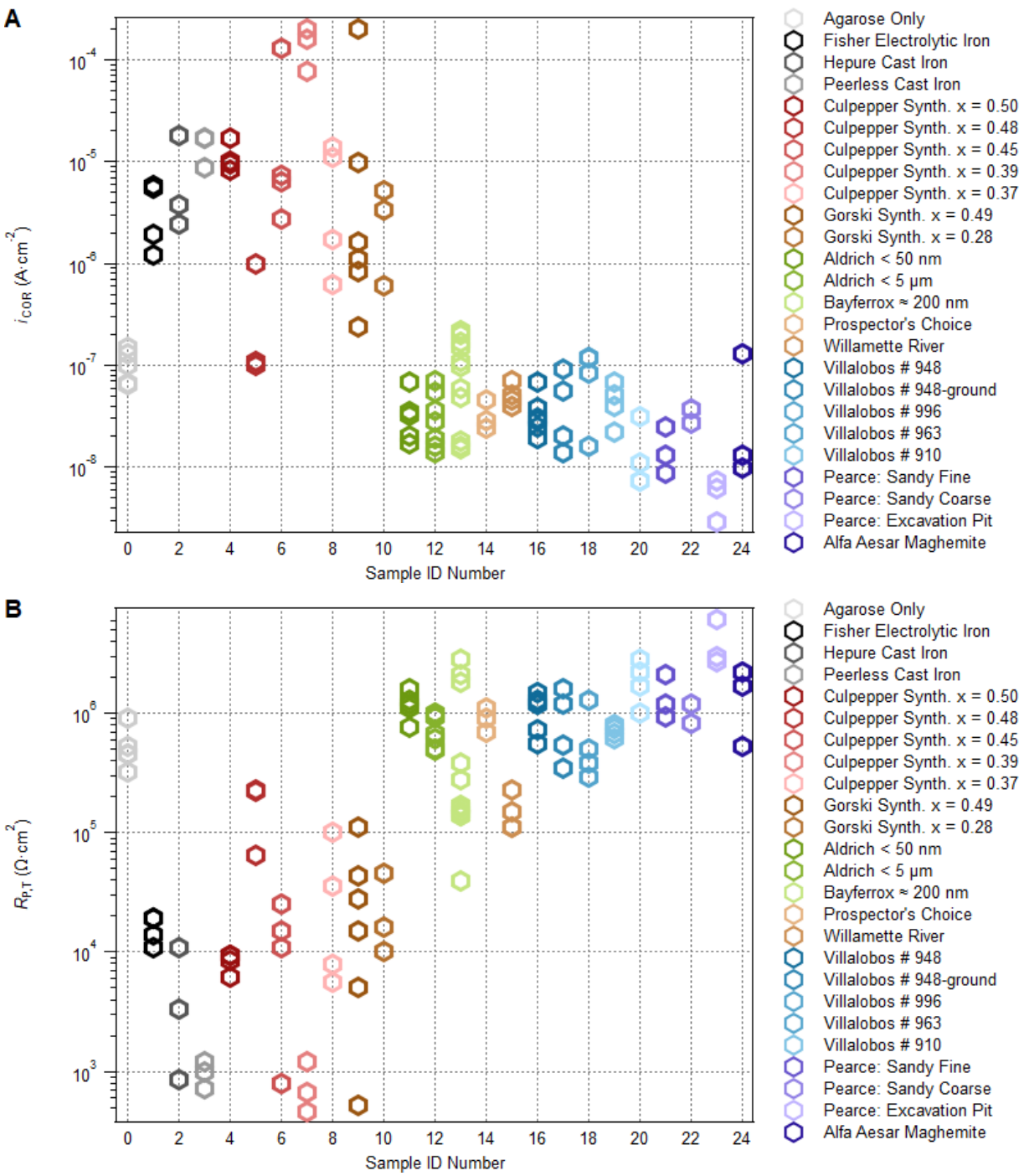

Figure 18. (A) corrosion current determined by Tafel analysis (B) polarization resistance determined by Tafel analysis

3.5 Non-electrochemical characterization

To advance the interpretation of the electrochemical results described above, additional characterizations were performed on the material's structure and composition. A variety of characterization methods can be useful for this purpose, as exemplified by prior studies on redox properties of nZVI,[52] iron oxides,[78] green rust,[79, 80] clays,[81] etc. In this study, we used just two bulk characterization methods: (*i*) XRD to verify that the magnetically-separated material from river sediments was magnetite, and (*ii*) acid-digestion followed by colorimetric determination of ferrous and total iron to determine stoichiometric ratio (*x*). A few other physical properties (particle size and specific surface area) were determined and are summarized in **Table 1** of Appendix B, but more advanced characterization methods were left for future work.

The XRD analyses (**Figure 24**, Appendix B) confirmed that all samples—including the commercial and magnetically separated materials, but excluding ZVI—were predominately of the magnetite family (including magnetite, maghemite, and magnetite substituted with titanium or magnesium for Fe^{3+} because these closely-related phases can not be distinguished reliably by XRD[82-84]). The three samples that had not been previously characterized at all were analyzed by SEM and EDS (**Figure 25**-**Figure 27**, Appendix B). The SEMs showed that the Prospector's Choice sample was relatively diverse in grain size and shape, but the two samples from the Willamette River were notably uniform in morphology. Overall, the particles were blocky with irregular facets suggesting crystal faces, which is consistent with weathered detrital magnetite in other studies,[22, 85-87] and somewhat different than laboratory synthesized magnetite, which tends to feature a more regular and stable crystalline [111] structure.[88, 89] EDS performed on randomly-selected spots gave the elemental compositions tabulated in Part B of **Figure 25**-**Figure 27** and summarized in **Figure 28** (Appendix B). The EDS data show that (*i*) the amount of iron near the surface varied greatly (1-82%) between spots (faces), (*ii*) oxygen varied much less (9-52%), and (*iii*) the third most variable element was Ti (0-32%). The magnetically separated material from Prospector's Choice showed very little Ti content, and the non-magnetite impurities appeared to be mostly aluminosilicates. Both size fractions of magnetically separated material from local Willamette river sediment had significant Ti content along with Si and Al.

At the outset of this study, it was hypothesized the Fe/Fe stoichiometry (*x*) would be a controlling factor in the electrochemical properties of magnetite, so we measured *x* by a acid digestion and colorimetric method that was optimized and validated in previous work.[61-64] In that

work, it was determined that this protocol gave results comparable to Moessbauer spectroscopy, despite being based on very different procedures and principles; and none of the samples used in this work came from sulfidic conditions.[90] One advantage of the protocol used here is that the digestion process gave some qualitative indications of sample purity. So, while the commercially purchased and collaborator synthesized magnetites dissolved fully and readily in 5 M HCl, the Bayferrox magnetite left a fluffy black residue that was unaffected by a magnet. Previous studies have noted the impurity of Bayferrox magnetite, and suggested it was mostly SiO_2 and Al_2O_3 (< 3%), based on XRD analysis,[91] but other studies using this material have ignored its impurity.[39, 92] For most of the magnetically-separated samples, 12 M HCl was needed to dissolve all the magnet-responsive material, after which there was a small residue of undigested white sandy material. This includes the sample Villalobos 948, although the "extra grind" of this sample (Villalobos "948-fine") left a fluffy black residue which is more similar to the result seen with the Bayferrox sample.

Since the residues that could not be dissolved presumably were not iron minerals, this material should not bias the determination of *x*, and control experiment (not shown) indicated that the method was accurate and precise. The resulting stoichiometries measured on of all magnetite samples studied are documented in **Table 2** of Appendix B, and summarized in **Figure 19**. The error bars in **Figure 19** result from three or more fully independent measurements on each sample (unless otherwise noted), and suggest an overall relative standard deviation of about 6%, which is small compared with the total range of measured *x* values. **Figure 19** also includes the data for *x* that were available from other sources (red squares), and they are consistent with the new data (blue circles), except for one outlier (Pearce: Sandy Fine). The outlier may or may not be spurious because it also fits the overall trend of new *x* values being lower than old values, which is the expected result of aging and/or oxidation over significant time periods. The highest values of *x* are for the magnetically-separated materials (Peña Colorada mine and Willamette river), with the former presumably representing naturally pure, stoichiometric magnetite without significant aging and the latter being Ti-enriched magnetite (**Figure 25**-**Figure 27**) from relatively reducing environmental conditions. Most of lowest values of *x* are from the commercial magnetite samples suggesting they were more oxidized than any of the magnetically separated materials. This is consistent with oxidation during aerobic storage, which might have

been accelerated by their relatively small particle size (all samples with even smaller particle size were stored anaerobically.

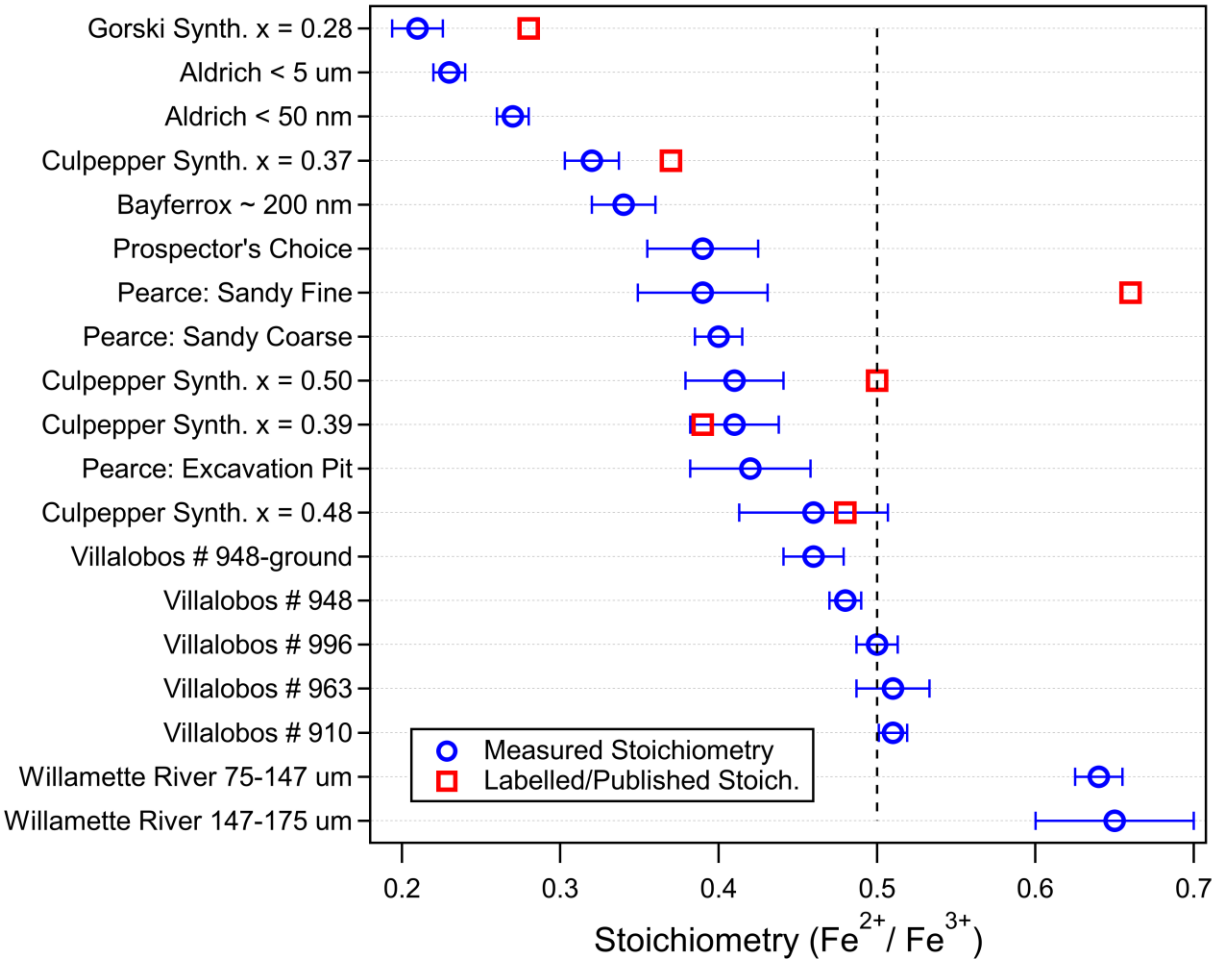

Figure 19. Stoichiometry determined by acid dissolution of samples, error bars are standard deviation of averaged multiple preparations. Y-axis is sorted by measured stoichiometry.

Using the measured values of *x* for each sample (**Table 2**) and corresponding values of the various electrochemical properties (**Table 2** and **Table 3**) an extensive correlation analysis was performed (**Figure 20**). While no combination of properties produced an overall correlation indicative of the hypothesized structure-property relationship, the data form well-defined clusters based on material category. One consistent pattern in the distribution of these clusters is that the commerically-purchased and magnetically-seperated samples give similar values of E_{OC}, $\Delta E_{LSV/OC}$, $R_{P,R}$, and i_{COR} (regardless of *x*), whereas the samples synthesized by collaborators generally cluster at higher or lower values. This difference is unsurprising because freshly

precipitated minerals often are found to differ from aged minerals,[93, 94] but the specific factor(s) responsible for the effect in this case are unclear.

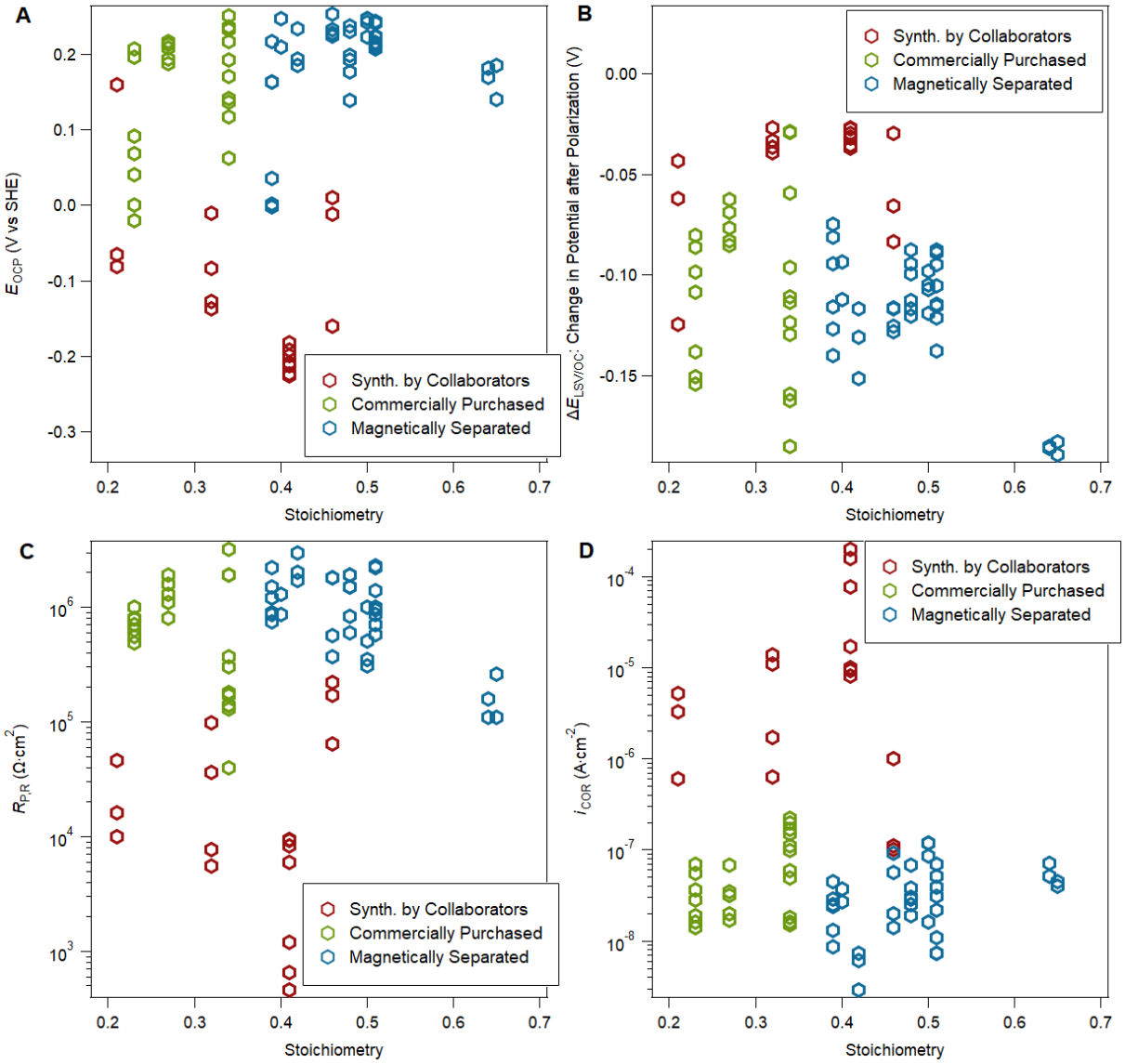

Figure 20. Correlation analysis of measured magnetite stoichiometry (*x*) vs (A) E_{OC}, (B) $\Delta E_{LSV/OC}$, (C) $R_{P,R}$, (D) i_{CORR}.

Chapter 4: Conclusions

Redox reactions at mineral-water interfaces are among the most interesting chemical processes that occur in aquatic environmental systems, primarily because of their importance in soils, sediments, aquifers, rivers, lakes, and water treatment systems, but secondarily because they are challenging to study and understand.[95] A major aspect of this challenge is the measurement and interpretation of redox potentials, especially those that apply to the mineral-water interface in environmental systems that are heterogeneous and dynamic. For such complex systems, measured redox potentials are necessary, which can be easy to implement but difficult to interpret. Many aspects of this dilemma are illustrated by a recent study of redox potentials measured with Pt working electrodes in suspensions of fine-grained iron and iron oxides.[59] One broadly-significant conclusion from that study is that such measurements are mixed potentials that reflect not only specific redox couples, but also the influence of much less well-defined factors such as particle (dis)aggregation and deposition onto the electrode surface.

The approach taken in this study eliminates the complications caused by colloidal materials by consolidating the analyte material into a uniformly packed bed working electrode. Although the response of this electrode could be complicated by other factors (e.g., discontinuities at interparticle interfaces and gradients in pore water chemistry), the conditions used in this study appear to have produced electrodes with response that is dominated by the original sample material. The resulting apparent potentials are mixed potentials in that they reflect the overall bulk and interfacial composition of the material, but the relative contribution of each redox couple is not known. To clarify this, we calculated formal potentials for relevant redox couples using thermodynamic data from the literature and solution conditions for our experiments (**Table 5**) and compared them to the potentials we measured for each sample in **Figure 21**.

As expected for a mixed potential, the calculated potentials bracket the measured potentials, but the aged magnetite samples (commercially-purchased and magnetically separated) align near or above the redox couples involving magnetite that have the most positive calculated potentials (e.g., α-FeOOH/Fe_3O_4). This suggests the measured mixed potentials are dominated by these redox couples and not the more commonly invoked half-reactions like Fe_3O_4/Fe^{2+}. Another

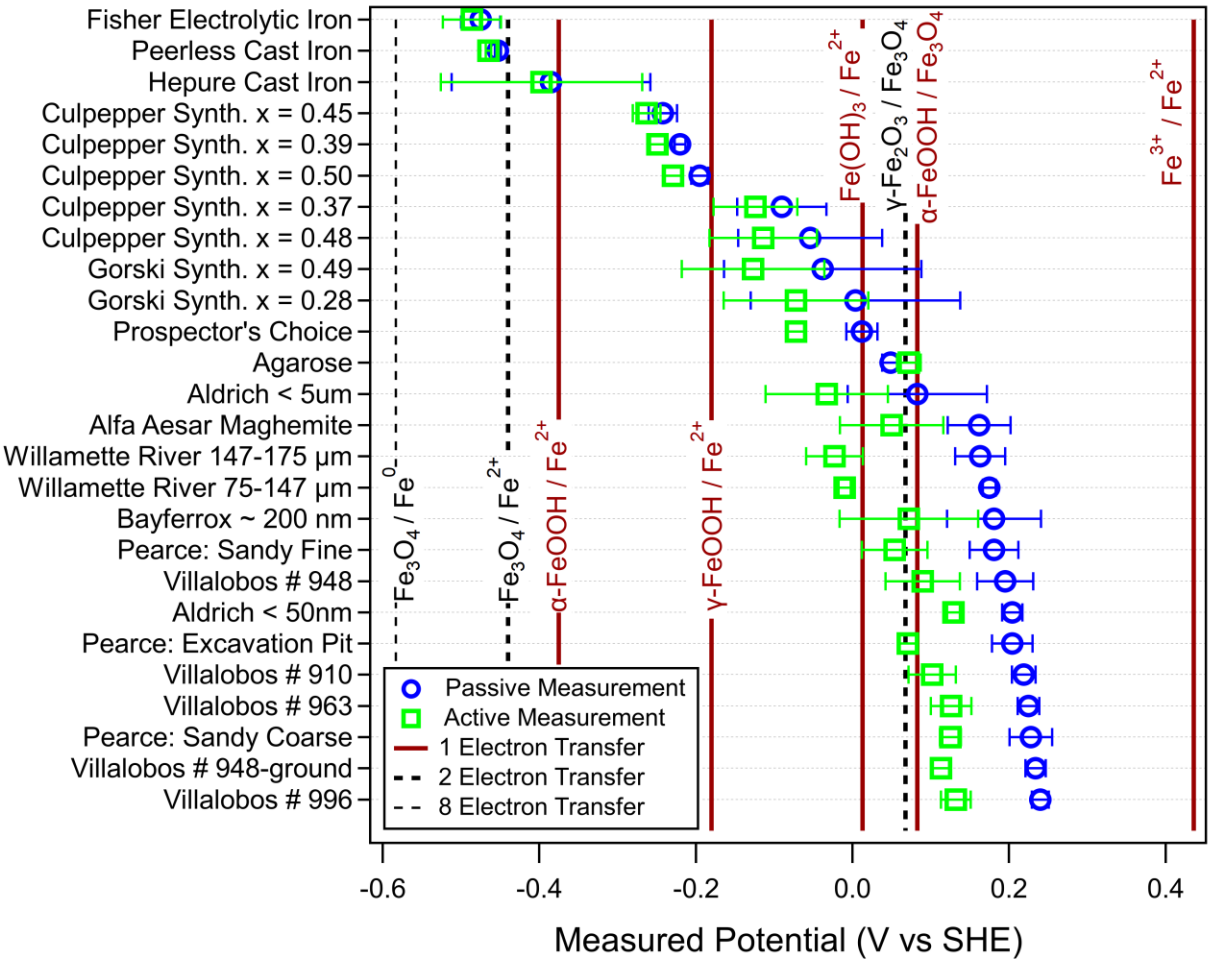

Figure 21. Passive (Open Circuit Potential) and Active (Linear Sweep Voltammetry) measured potentials for all samples in study; error bars are standard deviation of averaged multiple preparations. E_H at pH 8.4 for relevant redox couples are plotted for comparison, original values and calculated values can be found in **Table 5**.

possibly is that the mixed potential is shifted to more positive values by half-reactions not represented here, but all of the likely candidates (e.g., those involving dissolved oxygen) should be negligible. An additional consideration is that one-electron half-reactions (red lines in **Figure 21**) generally have higher exchange currents than multi-electron half-reactions,[96, 97] and therefore are likely to dominate the measured mixed potential, which is consistent with the alignment of calculated and measured values in **Figure 21**.

The thermodynamic potentials in **Figure 21** were calculated assuming the dissolved Fe^{2+} concentration was 10^{-7} M (**Table 5**), which was selected based on side experiments measuring the release of Fe^{2+} from Bayferrox magnetite (data not shown). Exploratory experiments

performed early in this study showed little effect of adding Fe^{2+} to the electrolyte, so all the measurements reported here were performed without added Fe^{2+}. This leaves only dissolution of the sample materials during the electrochemical measurements as a source of dissolved Fe^{2+}, and this is expected to be minimal under the conditions of the experiments reported here. Nevertheless, some (re)adsorption of Fe^{2+} is inevitable, especially because (*i*) our system is buffered at pH 8.4, which is in the pH range where magnetite has a significant affinity for Fe^{2+},[98] and (*ii*) it is more favorable for Fe^{2+} that becomes oxidized at the iron oxide surface to add to the existing lattice rather than form new colloidal material such as amorphous ferrihydrite.[78, 99, 100] The fate of Fe^{2+} that adsorbs to iron oxides has been the subject of many recent studies,[101-104] and future work using the PDEv2 might contribute to this subject (e.g., by preparing electrodes with different initial concentration of Fe^{2+} in the pore-space), but this was not included within the scope of the current study.

A unique aspect of the experiments reported here is the quantification of how much magnetite potential shifts upon polarization ($\Delta E_{LSV/OC}$), and this effect may provide insight into how the redox properties of minerals vary with mineral composition. For example, even though the 2-electron reduction of maghemite to magnetite should not produce sufficient exchange current to directly influence E_{OC}, cathodic polarization of the electrode will make this reaction more favorable, which could account for some of the negative shift in $E_{LSV/OC}$ upon polarization of the commercial and magnetically separated magnetite electrodes. Other researchers have reported similar effects of cathodic polarization,[105] and attributed it to the reduction of unstable oxide layers[106] or partial/total removal of a passive surface film.[107] Alternatively, the cathodic polarization effect could be an artifact of disrupted charging current during polarization,[108] but our ability to use this value to approximate the corrosion current (i_{CALC}) favors the interpretation of this effect in terms of interfacial redox processes involving iron oxides. In future work, measurements of $\Delta E_{LSV/OC}$ could be compared with other approaches to quantifying the electron accepting capacities of reducing materials,[109] and this might provide further insight into the role of iron oxides in buffering electron donor/acceptor processes in biogeochemical systems.

The practical motivation for this work was originally focused on developing relationships that could predict contaminant reduction from reducing material properties (i.e., quantitative property-activity relationships, or QPARs). For this, quantitative descriptors are needed for the reducing materials, and a powerful source of such descriptor data might be electrochemical

measurements made using PDEs made from these materials. A preliminary test of this approach using reduction of nitrobenzene as the contaminant reaction yielded promising correlations,[21] but subsequent efforts raised fundamental questions about how the PDE electrode response relates to material structure (e.g., E_{OC} vs. x), and what electrochemical properties might be most predictive of contaminant reduction rates (e.g., E_{OC} or i_{COR}). Other studies have shown good correlations between (*i*) magnetite stoichiometry (x) and the kinetics of nitrobenzene reduction[89, 110] or U^{VI} reduction,[111] (*ii*) between redox potentials of mineral suspensions determined potentiometrically with electron-transfer mediators and nitrobenzene reduction rates,[37] and (*iii*) between redox potentials of various iron mineral suspensions determined spectrophotometrically with chemical redox probes (CRPs) and the rates of contaminant nitro reduction and dechlorination.[39] However, this study shows that freshly synthesized magnetite can have lower E and R_P with higher i_{COR} (all of which suggest faster reduction of contaminants), even when prepared with low stoichiometry (which would suggest slower contaminant reduction rates). The overall implication of this inconsistency is that predicting contaminant reduction rates from mineral properties is likely to require more sophisticated models, perhaps including multiple descriptors (e.g., to account for thermodynamic, kinetics, and capacity factors) and/or more holistic characterization of dynamic system characteristics (like the "reactive mineral intermediate" phases implicated in several recent studies[112, 113]).

References

1. Sparks, D. L., *Environmental Soil Chemistry*. Elsevier: 2003.
2. Brantley, S.; White, T.; White, A.; Sparks, D.; Richter, D.; Pregitzer, K.; Derry, L.; Chorover, J.; Chadwick, O.; April, R., Frontiers in exploration of the Critical Zone: Report of a workshop sponsored by the National Science Foundation (NSF), October 24–26, 2005. *Newark, DE* **2006**, 30.
3. Usman, M.; Byrne, J. M.; Chaudhary, A.; Orsetti, S.; Hanna, K.; Ruby, C.; Kappler, A.; Haderlein, S. B., Magnetite and green rust: Synthesis, properties, and environmental applications of mixed-valent iron minerals. *Chem. Rev.* **2018**; DOI: 10.1021/acs.chemrev.7b00224.
4. Cornell, R. M.; Schwertmann, U., *The Iron Oxides: Structure, Properties, Reactions, Occurrences And Uses*. John Wiley & Sons: 2003.
5. Greenwood, N. N.; Earnshaw, A., Chemistry of the Elements. **1984**.
6. Palacin, S.; Hidber, P. C.; Bourgoin, J.-P.; Miramond, C.; Fermon, C.; Whitesides, G. M., Patterning with magnetic materials at the micron scale. *Chem. Mater.* **1996,** *8*, (6), 1316-1325.
7. Terris, B.; Thomson, T., Nanofabricated and self-assembled magnetic structures as data storage media. *J. Phys. D: Appl. Phys.* **2005,** *38*, (12), R199.
8. Frankel, R. B.; Bazylinski, D. A., Magnetotaxis and magnetic particles in bacteria. *Hyperfine Interact.* **1994,** *90*, (1), 135-142.
9. Pankhurst, Q.; Thanh, N.; Jones, S.; Dobson, J., Progress in applications of magnetic nanoparticles in biomedicine. *J. Phys. D: Appl. Phys.* **2009,** *42*, (22), 224001.
10. Ito, A.; Hibino, E.; Kobayashi, C.; Terasaki, H.; Kagami, H.; Ueda, M.; Kobayashi, T.; Honda, H., Construction and delivery of tissue-engineered human retinal pigment epithelial cell sheets, using magnetite nanoparticles and magnetic force. *Tissue Eng.* **2005,** *11*, (3-4), 489-496.
11. Kumar, C. S.; Mohammad, F., Magnetic nanomaterials for hyperthermia-based therapy and controlled drug delivery. *Adv. Drug Deliv. Rev.* **2011,** *63*, (9), 789-808.
12. He, Y.; Huang, L.; Cai, J.-S.; Zheng, X.-M.; Sun, S.-G., Structure and electrochemical performance of nanostructured Fe_3O_4/carbon nanotube composites as anodes for lithium ion batteries. *Electrochim. Acta* **2010,** *55*, (3), 1140-1144.
13. Qu, X.; Alvarez, P. J.; Li, Q., Applications of nanotechnology in water and wastewater treatment. *Water Res.* **2013,** *47*, (12), 3931-3946.
14. Kandemir, T.; Schuster, M. E.; Senyshyn, A.; Behrens, M.; Schlögl, R., The Haber–Bosch process revisited: on the real structure and stability of “ammonia iron” under working conditions. *Angew. Chem., Int. Ed.* **2013,** *52*, (48), 12723-12726.

15. Rahim Pouran, S.; Abdul Raman, A. A.; Wan Daud, W. M. A., Review on the application of modified iron oxides as heterogeneous catalysts in Fenton reactions. *J. Cleaner Prod.* **2014,** *64*, (0), 24-35; DOI: 10.1016/j.jclepro.2013.09.013.

16. Toney, M. F.; Davenport, A. J.; Oblonsky, L. J.; Ryan, M. P.; Vitus, C. M., Atomic structure of the passive oxide film formed on iron. *Phys. Rev. Lett.* **1997,** *79*, (21), 4282-4285; DOI: 10.1103/PhysRevLett.79.4282.

17. Yang, F.; Shi, B.; Gu, J.; Wang, D.; Yang, M., Morphological and physicochemical characteristics of iron corrosion scales formed under different water source histories in a drinking water distribution system. *Water Res.* **2012,** *46*, (16), 5423-5433.

18. Porsch, K.; Rijal, M. L.; Borch, T.; Troyer, L. D.; Behrens, S.; Wehland, F.; Appel, E.; Kappler, A., Impact of organic carbon and iron bioavailability on the magnetic susceptibility of soils. *Geochim. Cosmochim. Acta* **2014,** *128*, (0), 44-57; DOI: 10.1016/j.gca.2013.12.001.

19. Byrne, J. M.; Klueglein, N.; Pearce, C.; Rosso, K. M.; Appel, E.; Kappler, A., Redox cycling of Fe(II) and Fe(III) in magnetite by Fe-metabolizing bacteria. *Science* **2015,** *347*, (6229), 1473-1476; DOI: 10.1126/science.aaa4834.

20. Rodelli, D.; Jovane, L.; Roberts, A. P.; Cypriano, J.; Abreu, F.; Lins, U., Fingerprints of partial oxidation of biogenic magnetite from cultivated and natural marine magnetotactic bacteria using synchrotron radiation. *Environ. Microbiol. Rep.* **2018**; DOI: 10.1111/1758-2229.12644.

21. Gorski, C. A.; Nurmi, J. T.; Tratnyek, P. G.; Hofstetter, T. B.; Scherer, M. M., Redox behavior of magnetite: Implications for contaminant reduction. *Environ. Sci. Technol.* **2010,** *44*, (1), 55-60; DOI: 10.1021/es9016848.

22. Salazar-Camacho, C.; Villalobos, M.; Rivas-Sánchez, M. d. l. L.; Arenas-Alatorre, J.; Alcaraz-Cienfuegos, J.; Gutiérrez-Ruiz, M. E., Characterization and surface reactivity of natural and synthetic magnetites. *Chem. Geol.* **2013,** *347*, (0), 233-245; DOI: 10.1016/j.chemgeo.2013.03.017.

23. Latta, D. E.; Pearce, C. I.; Rosso, K. M.; Kemner, K. M.; Boyanov, M. I., Reaction of U^{VI} with titanium-substituted magnetite: Influence of Ti on U^{IV} speciation. *Environ. Sci. Technol.* **2013,** *47*, (9), 4121-4130; DOI: 10.1021/es303383n.

24. Vikesland, P. J.; Heathcock, A. M.; Rebodos, R. L.; Makus, K. E., Particle size and aggregation effects on magnetite reactivity toward carbon tetrachloride. *Environ. Sci. Technol.* **2007,** *41*, (15), 5277-5283.

25. Yuan, K.; Ilton, E. S.; Antonio, M. R.; Li, Z.; Cook, P. J.; Becker, U., Electrochemical and Spectroscopic Evidence on the One-Electron Reduction of U(VI) to U(V) on Magnetite. *Environ. Sci. Technol.* **2015,** *49*, (10), 6206-6213; DOI: 10.1021/acs.est.5b00025.

26. Yuan, K.; Renock, D.; Ewing, R. C.; Becker, U., Uranium reduction on magnetite: Probing for pentavalent uranium using electrochemical methods. *Geochim. Cosmochim. Acta* **2015,** *156*, 194-206; DOI: 10.1016/j.gca.2015.02.014.

27. Pasakarnis, T. S.; Boyanov, M. I.; Kemner, K. M.; Mishra, B.; O'Loughlin, E. J.; Parkin, G.; Scherer, M. M., Influence of Chloride and Fe(II) Content on the Reduction of Hg(II) by Magnetite. *Environ. Sci. Technol.* **2013,** *47*, (13), 6987-6994; DOI: 10.1021/es304761u.

28. Xu, Y.; Schoonen, M. A. A., The absolute energy positions of conduction and valence bands of selected semiconducting minerals. *Am. Mineral.* **2000,** *85*, 543-556.

29. Shuey, R., *Semiconducting ore minerals*. Elsevier: 2012; Vol. 4.

30. White, A. F.; Peterson, M. L.; Hochella, M. F., Jr., Electrochemistry and dissolution kinetics of magnetite and ilmenite. *Geochim. Cosmochim. Acta* **1994,** *58*, (8), 1859-75; DOI: 10.1016/0016-7037(94)90420-0.

31. Gedikoqlu, A., Mossbauer study of low temperature oxidation in natural magnetite. *Scripta Metallurgica* **1983,** *17*, (1), 45-48.

32. Van Velzen, A. J.; Dekkers, M. J., Low-temperature oxidation of magnetite in loess-paleosol sequences: a correction of rock magnetic parameters. *Studia geophysica et geodaetica* **1999,** *43*, (4), 357-375.

33. White, A. F.; Peterson, M. L., Reduction of aqueous transition metal species on the surfaces of Fe(II)-containing oxides. *Geochim. Cosmochim. Acta* **1996,** *60*, (20), 3799-3814; DOI: 10.1016/0016-7037(96)00213-X.

34. Castro, P. A.; Vago, E. R.; Calvo, E. J., Surface electrochemical transformations on spinel iron oxide electrodes in aqueous solutions. *J. Chem. Soc., Faraday Trans.* **1996,** *92*, (18), 3371-3379; DOI: 10.1039/ft9969203371.

35. Pearce, C. I.; Henderson, C. M. B.; Pattrick, R. A.; Laan, G. V. D.; Vaughan, D. J., Direct determination of cation site occupancies in natural ferrite spinels by L2, 3 X-ray absorption spectroscopy and X-ray magnetic circular dichroism. *Am. Mineral.* **2006,** *91*, (5-6), 880-893.

36. Gorski, C. A.; Edwards, R.; Sander, M.; Hofstetter, T. B.; Stewart, S. M., Thermodynamic characterization of iron oxide–aqueous Fe^{2+} redox couples. *Environ. Sci. Technol.* **2016,** *50*, (16), 8538-8547; DOI: 10.1021/acs.est.6b02661.

37. Stewart, S. M.; Hofstetter, T. B.; Joshi, P.; Gorski, C. A., Linking thermodynamics to pollutant reduction kinetics by Fe^{2+} bound to iron oxides. *Environ. Sci. Technol.* **2018**; DOI: 10.1021/acs.est.8b00481.

38. Levar, C. E.; Hoffman, C. L.; Dunshee, A. J.; Toner, B. M.; Bond, D. R., Redox potential as a master variable controlling pathways of metal reduction by Geobacter sulfurreducens. *ISME J.* **2017,** *11*, (3), 741-752; DOI: 10.1038/ismej.2016.146.

39. Fan, D.; Bradley, M.; Hinkle, A. W.; Johnson, R. L.; Tratnyek, P. G., Chemical reactivity probes for assessing abiotic natural attenuation by reducing iron minerals. *Environ. Sci. Technol.* **2016,** *50*, (4), 1868-1876; DOI: 10.1021/acs.est.5b05800.

40. Sander, M.; Hofstetter, T. B.; Gorski, C. A., Electrochemical analyses of redox-active iron minerals: A review of nonmediated and mediated approaches. *Environ. Sci. Technol.* **2015**; DOI: 10.1021/acs.est.5b00006.

41. Haruyama, S.; Masamura, K., The dissolution of magnetite in acidic perchlorate solutions. *Corros. Sci.* **1978,** *18*, (4), 263-274.

42. Allen, P. D.; Hampson, N. A.; Bignold, G. J., The electrodissolution of magnetite. Part I. The electrochemistry of iron oxide (Fe_3O_4/C) discs - potentiodynamic experiments. *J. Electroanal. Chem. Interfac. Electrochem.* **1979,** *99*, (3), 299-309; DOI: 10.1016/0368-1874(79)87061-6.

43. Allen, P. D.; Hampson, N. A.; Bignold, G. J., The electrodissolution of magnetite. Part II. The oxidation of bulk magnetite. *J. Electroanal. Chem. Interfac. Electrochem.* **1980,** *111*, (2-3), 223-33; DOI: 10.1016/0368-1874(80)80255-3.

44. Kuznetsov, Y. I.; Vershok, D. B., Impedance of magnetite-coated steel electrodes. *Russian Journal of Electrochemistry* **2001,** *37*, (3), 261-265.

45. Joiret, S.; Keddam, M.; Novoa, X. R.; Perez, M. C.; Rangel, C.; Takenouti, H., Use of EIS, ring-disk electrode, EQCM and Raman spectroscopy to study the film of oxides formed on iron in 1 M NaOH. *Cem. Concr. Compos.* **2002,** *24*, (1), 7-15; DOI: 10.1016/S0958-9465(01)00022-1.

46. Allen, P.; Hampson, N.; Bignold, G., The effect of the potential on the dissolution of magnetite. *Surface Technology* **1981,** *12*, (2), 199-204.

47. Wu, N.-L.; Wang, S.-Y.; Han, C.-Y.; Wu, D.-S.; Shiue, L.-R., Electrochemical capacitor of magnetite in aqueous electrolytes. *J. Power Sources* **2003,** *113*, (1), 173-178.

48. Shi, Z.; Liu, M., Electrical and electrochemical analysis of nanophase materials. In *Characterization of Nanophase Materials*, Wang, Z. L., Ed. Wiley: 2000; pp 165-196.

49. Scholz, F.; Schröder, U.; Gulaboski, R., *Electrochemistry of Immobilized Particles and Droplets*. Springer: Berlin, 2005.

50. Doménech-Carbó, A., *Electrochemistry of Porous Materials*. CRC Press, 2010; p 312.

51. Nurmi, J. T.; Bandstra, J. Z.; Tratnyek, P. G., Packed powder electrodes for characterizing the reactivity of granular iron in borate solutions. *J. Electrochem. Soc.* **2004,** *151*, (6), B347-B353.

52. Nurmi, J. T.; Tratnyek, P. G.; Sarathy, V.; Baer, D. R.; Amonette, J. E.; Pecher, K.; Wang, C.; Linehan, J. C.; Matson, D. W.; Penn, R. L.; Driessen, M. D., Characterization and properties of metallic iron nanoparticles: Spectroscopy, electrochemistry, and kinetics. *Environ. Sci. Technol.* **2005,** *39*, (5), 1221-1230; DOI: 10.1021/es049190u.

53. Nurmi, J. T.; Tratnyek, P. G., Electrochemical studies of packed iron powder electrodes: Effects of common constituents of natural waters on corrosion potential. *Corros. Sci.* **2008,** *50*, (1), 144-154; DOI: 10.1016/j.corsci.2007.06.016

54. Sarathy, V.; Tratnyek, P. G.; Nurmi, J. T.; Baer, D. R.; Amonette, J. E.; Chun, C.; Penn, R. L.; Reardon, E. J., Aging of iron nanoparticles in aqueous solution: effects on structure and reactivity. *J. Phys. Chem. C* **2008,** *112*, (7), 2286-2293; DOI: 10.1021/jp0777418.

55. Nurmi, J. T.; Sarathy, V.; Tratnyek , P. G.; Baer, D. R.; Amonette, J. E.; Linehan, J. C.; Karkamkar, A., Recovery of iron/iron oxide nanoparticles from aqueous media: A

comparison of methods and their effects. *J. Nanoparticle Res.* **2011,** *13*, (5), 1937-1952; DOI: 10.1007/s11051-010-9946-x.

56. Turcio-Ortega, D.; Fan, D.; Tratnyek, P. G.; Kim, E.-J.; Chang, Y.-S., Reactivity of Fe/FeS nanoparticles: Electrolyte composition effects on corrosion electrochemistry. *Environ. Sci. Technol.* **2012,** *46*, (22), 12484-12492; DOI: 10.1021/es303422w.

57. Gu, Y.; Wang, B.; He, F.; Bradley, M. J.; Tratnyek, P. G., Mechanochemically sulfidated microscale zero valent iron: Pathways, kinetics, mechanism, and efficiency of trichloroethylene dechlorination. *Environ. Sci. Technol.* **2017**; DOI: 10.1021/acs.est.7b03604.

58. Tratnyek, P. G.; Salter-Blanc, A. J.; Nurmi, J. T.; Amonette, J. E.; Liu, J.; Wang, C.; Dohnalkova, A.; Baer, D. R., Reactivity of zerovalent metals in aquatic media: Effects of organic surface coatings. In *Aquatic Redox Chemistry*, Tratnyek, P. G.; Grundl, T. J.; Haderlein, S. B., Eds. American Chemical Society: Washington, DC, 2011; Vol. 1071, pp 381-406, DOI: 10.1021/bk-2011-1071.ch018.

59. Shi, Z.; Nurmi, J. T.; Tratnyek, P. G., Effects of nano zero-valent iron (nZVI) on oxidation-reduction potential (ORP). *Environ. Sci. Technol.* **2011,** *45*, (5), 1586-1592; DOI: 10.1021/es103185t.

60. Masue-Slowey, Y.; Kocar, B. D.; Bea Jofré, S. A.; Mayer, K. U.; Fendorf, S., Transport implications resulting from internal redistribution of arsenic and iron within constructed soil aggregates. *Environ. Sci. Technol.* **2011,** *45*, (2), 582-588.

61. Viollier, E.; Inglett, P. W.; Hunter, K.; Roychoudhury, A. N.; Van Cappellen, P., The ferrozine method revisited: Fe(II)/Fe(III) determination in natural waters. *Appl. Geochem.* **2000,** *15*, (6), 785-790.

62. Chao, T. T.; Zhou, L., Extraction techniques for selective dissolution of amphorous iron oxides from soils and sediments. *Soil Sci. Soc. Am. J.* **1983,** *47*, (2), 225-232; DOI: 10.2136/sssaj1983.03615995004700020010x.

63. Gibbs, C. R., Characterization and application of FerroZine iron reagent as a ferrous iron indicator. *Anal. Chem.* **1976,** *48*, (8), 1197-1200.

64. Stookey, L. L., Ferrozine—A new spectrophotometric reagent for iron. *Anal. Chem.* **1970,** *42*, (7), 779-781.

65. Wang, C. M.; Baer, D. R.; Amonette, J. E.; Engelhard, M. H.; Qiang, Y.; Antony, J., Morphology and oxide shell structure of iron nanoparticles grown by sputter-gas-aggregation. *Nanotechnology* **2007,** *18*, 255-603.

66. Kim, H.-S.; Ahn, J.-Y.; Hwang, K.-Y.; Kim, I.-K.; Hwang, I., Atmospherically stable nanoscale zero-valent iron particles formed under controlled air contact: Characteristics and reactivity. *Environ. Sci. Technol.* **2010,** *44*, (5), 1760-1766; DOI: 10.1021/es902772r.

67. Mansfeld, F., Fundamental aspects of the polarization resistance technique—The early days. *J. Solid State Electrochem.* **2009,** *13*, (4), 515-520.

68. Scherer, M. M.; Westall, J. C.; Ziomek-Moroz, M.; Tratnyek, P. G., Kinetics of carbon tetrachloride reduction at an oxide-free iron electrode. *Environ. Sci. Technol.* **1997,** *31*, (8), 2385-2391; DOI: 10.1021/es960999j.

69. Bard, A. J.; Faulkner, L. R., *Electrochemical Methods. Fundamentals and Applications*. Wiley: New York, 2001; p 833.

70. Farrell, J.; Melitas, N.; Kason, M.; Li, T., Electrochemical and column investigation of iron-mediated reductive dechlorination of trichloroethylene and perchloroethylene. *Environ. Sci. Technol.* **2000,** *34*, (12), 2549-2556.

71. Mansfeld, F., Simultaneous determination of instantaneous corrosion rates and Tafel slopes from polarization resistance measurements. *J. Electrochem. Soc.* **1973,** *120*, (4), 515-18; DOI: 10.1149/1.2403489.

72. Stern, M.; Geary, A. L., Electrochemical polarization. *J. Electrochem. Soc.* **1957,** *104*, (1), 56-63.

73. Liao, L.; Wang, S.; Xiao, J.; Bian, X.; Zhang, Y.; Scanlon, M. D.; Hu, X.; Tang, Y.; Liu, B.; Girault, H. H., A nanoporous molybdenum carbide nanowire as an electrocatalyst for hydrogen evolution reaction. *Energy Environ. Sci.* **2014,** *7*, (1), 387-392.

74. McCafferty, E., Validation of corrosion rates measured by the Tafel extrapolation method. *Corros. Sci.* **2005,** *47*, (12), 3202-3215.

75. Soderberg, J. N.; Co, A. C.; Sirk, A. H. C.; Birss, V. I., Impact of porous electrode properties on the electrochemical transfer coefficient. *J. Phys. Chem. B* **2006,** *110*, (21), 10401-10410; DOI: 10.1021/jp060372f.

76. Atia, A.; Saleh, M., Inhibition of acid corrosion of steel using cetylpyridinium chloride. *J. Appl. Electrochem.* **2003,** *33*, (2), 171-177.

77. Abdel-Gaber, A.; Abd-El-Nabey, B.; Sidahmed, I.; El-Zayady, A.; Saadawy, M., Inhibitive action of some plant extracts on the corrosion of steel in acidic media. *Corros. Sci.* **2006,** *48*, (9), 2765-2779.

78. Larese-Casanova, P.; Kappler, A.; Haderlein, S. B., Heterogeneous oxidation of Fe(II) on iron oxides in aqueous systems: Identification and controls of Fe(III) product formation. *Geochim. Cosmochim. Acta* **2012,** *91*, 171-186; DOI: 10.1016/j.gca.2012.05.031.

79. Legrand, L.; Maksoub, R.; Sagon, G.; Lecomte, S.; Dallas, J. P.; Chausse, A., Electroanalytical and kinetic investigations on the carbonate green rust-Fe(III) redox system. *J. Electrochem. Soc.* **2003,** *150*, (2), B45-B51.

80. Antony, H.; Legrand, L.; Chaussé, A., Carbonate and sulphate green rusts—mechanisms of oxidation and reduction. *Electrochim. Acta* **2008,** *53*, (24), 7146-7156; DOI: 10.1016/j.electacta.2008.05.008.

81. Gorski, C. A.; Klupfel, L.; Voegelin, A.; Sander, M.; Hofstetter, T. B., Redox properties of structural Fe in clay minerals. 2. Electrochemical and spectroscopic characterization of electron transfer irreversibility in ferruginous smectite, SWa-1. *Environ. Sci. Technol.* **2012,** *46*, (17), 9369-9377; DOI: 10.1021/es302014u.

82. Janot, R.; Guérard, D., One-step synthesis of maghemite nanometric powders by ball-milling. *Journal of Alloys and Compounds* **2002,** *333*, (1-2), 302-307.

83. Schimanke, G.; Martin, M., In situ XRD study of the phase transition of nanocrystalline maghemite (γ-Fe_2O_3) to hematite (α-Fe_2O_3). *Solid State Ionics* **2000,** *136*, 1235-1240.

84. Van Oorschot, I.; Dekkers, M., Dissolution behaviour of fine-grained magnetite and maghemite in the citrate–bicarbonate–dithionite extraction method. *Earth Planet. Sci. Lett.* **1999,** *167*, (3-4), 283-295.

85. Baer, D. R.; Grosz, A. E.; Ilton, E. S.; Krupka, K. M.; Liu, J.; Penn, R. L.; Pepin, A., Separation, characterization and initial reaction studies of magnetite particles from Hanford sediments. *Physics and Chemistry of the Earth* **2010,** *35*, (6-8), 233-241; DOI: 10.1016/j.pce.2010.04.010.

86. Pearce, C. I.; Liu, J.; Baer, D. R.; Qafoku, O.; Heald, S. M.; Arenholz, E.; Grosz, A. E.; McKinley, J. P.; Resch, C. T.; Bowden, M. E.; Engelhard, M. H.; Rosso, K. M., Characterization of natural titanomagnetites ($Fe_{3-x}Ti_xO_4$) for studying heterogeneous electron transfer to Tc(VII) in the Hanford subsurface. *Geochim. Cosmochim. Acta* **2014,** *128*, (0), 114-127; DOI: 10.1016/j.gca.2013.12.010.

87. Villacís-García, M.; Villalobos, M.; Gutiérrez-Ruiz, M., Optimizing the use of natural and synthetic magnetites with very small amounts of coarse Fe(0) particles for reduction of aqueous Cr(VI). *J. Hazard. Mater.* **2015,** *281*, 77-86.

88. Sato, J.; Kobayashi, M.; Kato, H.; Miyazaki, T.; Kakihana, M., Hydrothermal synthesis of magnetite particles with uncommon crystal facets. *J. Asian Ceram. Soc.* **2014,** *2*, (3), 258-262.

89. Gorski, C. A.; Scherer, M. M., Influence of magnetite stoichiometry on Fe^{II} uptake and nitrobenzene reduction. *Environ. Sci. Technol.* **2009,** *43*, (10), 3675-3680.

90. Kwon, M. J.; Yang, J.-S.; Shim, M. J.; Boyanov, M. I.; Kemner, K. M.; O'Loughlin, E. J., Acid extraction overestimates the total Fe(II) in the presence of iron (hydr)oxide and sulfide minerals. *Environ. Sci. Technol. Lett.* **2014**; DOI: 10.1021/ez500152h.

91. Guzmán, G.; Barrón, V.; Gómez, J. A., Evaluation of magnetic iron oxides as sediment tracers in water erosion experiments. *Catena* **2010,** *82*, (2), 126-133.

92. Chen, S.; Fan, D.; Tratnyek, P. G., Novel contaminant transformation pathways by abiotic reductants. *Environ. Sci. Technol. Lett.* **2014,** *1*, (10), 432-436; DOI: 10.1021/ez500268e.

93. de Vicente, I.; Huang, P.; Andersen, F. Ø.; Jensen, H. S., Phosphate adsorption by fresh and aged aluminum hydroxide. Consequences for lake restoration. *Environ. Sci. Technol.* **2008,** *42*, (17), 6650-6655.

94. Shuman, L., Adsorption of Zn by Fe and Al Hydrous Oxides as Influenced by Aging and pH 1. *Soil Sci. Soc. Am. J.* **1977,** *41*, (4), 703-706.

95. Grundl, T. J.; Haderlein, S. P.; Nurmi, J. T.; Tratnyek, P. G., Introduction to aquatic redox chemistry. In *Aquatic Redox Chemistry*, Tratnyek, P. G.; Grundl, T. J.; Haderlein, S. B., Eds.

American Chemical Society: Washington, DC, 2011; Vol. 1071, pp 1-14, DOI: 10.1021/bk-2011-1071.ch001.

96. Sigg, L., Redox potential measurements in natural waters: Significance: Concepts and problems. In *Redox: Fundamentals, Processes and Applications*, Schüring, J.; Schulz, H. D.; Fischer, W. R.; Böttcher, J.; Duijnisveld, W. H. M., Eds. Springer: Berlin, 2000; pp 1-12.

97. Galster, H., Technique of measurement, electrode processes and electrode treatment. In *Redox: Fundamentals, Processes and Applications*, Schüring, J.; Schulz, H. D.; Fischer, W. R.; Böttcher, J.; Duijnisveld, W. H. M., Eds. Springer: Berlin, 2000; pp 13-23.

98. Klausen, J.; Troeber, S. P.; Haderlein, S. B.; Schwarzenbach, R. P., Reduction of substituted nitrobenzenes by Fe(II) in aqueous mineral suspensions. *Environ. Sci. Technol.* **1995,** *29*, (9), 2396-2404; DOI: 10.1021/es00009a036.

99. Chun Chan, L.; Penn, R. L.; Arnold William, A., Kinetic and microscopic studies of reductive transformations of organic contaminants on goethite. *Environ. Sci. Technol.* **2006,** *40*, (10), 3299-304.

100. Weidler, P. G.; Hug, S. J.; Wetche, T. P.; Hiemstra, T., Determination of growth rates of (100) and (110) faces of synthetic goethite by scanning force microscopy. *Geochim. Cosmochim. Acta* **1998,** *62*, (21-22), 3407-3412.

101. Yanina, S. V.; Rosso, K. M., Linked reactivity at mineral-water interfaces through bulk crystal conduction. *Science* **2008,** *320*, 218-222; DOI: 10.1126/science.1154833.

102. Handler, R. M.; Beard, B. L.; Johnson, C. M.; Scherer, M. M., Atom exchange between aqueous Fe(II) and goethite: An Fe isotope tracer study. *Environ. Sci. Technol.* **2009,** *43*, (4), 1102-1107; DOI: 10.1021/es802402m.

103. Gorski, C. A.; Scherer, M. M., Fe^{2+} Sorption at the Fe oxide-water interface: A revised conceptual framework. In *Aquatic Redox Chemistry*, Tratnyek, P. G.; Grundl, T. J.; Haderlein, S. B., Eds. American Chemical Society: Washington, DC, 2011; Vol. 1071, pp 315-343, DOI: 10.1021/bk-2011-1071.ch015.

104. Gorski, C. A.; Handler, R. M.; Beard, B. L.; Pasakarnis, T.; Johnson, C. M.; Scherer, M. M., Fe atom exchange between aqueous fe2+ and magnetite. *Environ. Sci. Technol.* **2012,** *46*, (22), 12399-12407; DOI: 10.1021/es204649a.

105. de Souza, F. S.; Spinelli, A., Caffeic acid as a green corrosion inhibitor for mild steel. *Corros. Sci.* **2009,** *51*, (3), 642-649.

106. Bertrand, G.; Mahdjoub, H.; Meunier, C., A study of the corrosion behaviour and protective quality of sputtered chromium nitride coatings. *Surface and Coatings Technology* **2000,** *126*, (2-3), 199-209.

107. de Assis, S. L.; Wolynec, S.; Costa, I., Corrosion characterization of titanium alloys by electrochemical techniques. *Electrochim. Acta* **2006,** *51*, (8-9), 1815-1819.

108. Zhang, X. L.; Jiang, Z. H.; Yao, Z. P.; Song, Y.; Wu, Z. D., Effects of scan rate on the potentiodynamic polarization curve obtained to determine the Tafel slopes and corrosion current density. *Corros. Sci.* **2009,** *51*, (3), 581-587; DOI: 10.1016/j.corsci.2008.12.005.

109. Gorski, C. A.; Aeschbacher, M.; Soltermann, D.; Voegelin, A.; Baeyens, B.; Marques Fernandes, M.; Hofstetter, T. B.; Sander, M., Redox properties of structural Fe in clay minerals. 1. Electrochemical quantification of electron-donating and -accepting capacities of smectites. *Environ. Sci. Technol.* **2012,** *46*, (17), 9360-9368; DOI: 10.1021/es3020138.

110. Gorski, C. A. Redox behavior of magnetite in the environment: Moving towards a semiconductor model. 2009.

111. Latta, D. E.; Gorski, C. A.; Boyanov, M. I.; O'Loughlin, E. J.; Kemner, K. M.; Scherer, M. M., Influence of magnetite stoichiometry on U^{VI} reduction. *Environ. Sci. Technol.* **2012,** *46*, (2), 778-786; DOI: 10.1021/es2024912.

112. Culpepper, J.; Scherer, M.; Robinson, T.; Neumann, A.; Cwiertny, D.; Latta, D., Reduction of PCE and TCE by magnetite revisited. *Environ. Sci. Proc. Impacts* **2018,** *20*, (10), 1340-1349 DOI: 10.1039/c8em00286j.

113. Qin, H.; Guan, X.; Bandstra, J. Z.; Johnson, R. L.; Tratnyek, P. G., Modeling the kinetics of hydrogen formation by zerovalent iron: Effects of sulfidation on micro- and nano-scale particles. *Environ. Sci. Technol.* **2018,** *52*, (23), 13887-13896; DOI: 10.1021/acs.est.8b04436.

Appendix A: Method details and development

Electrochemical Cell and iR Drop. The electrochemical cell was enclosed in a Faraday cage (**Figure 2B**), covered with a lid wrapped in aluminum foil. Both materials exhibited low resistance (approximately 100 mΩ) when tested with a multimeter. The cage was grounded to the potentiostat. The Faraday cage was shown to reduce noise in polarization experiments with low current output, and therefore was used throughout all experiments.

The current output was low for most electrode preparations (< 10 μA), so there was no need to compensate for an iR drop or to use a Luggin capillary.[1] The iR drop for each electrode preparation was calculated by multiplying the solution resistance (from impedance spectroscopy measurements, not shown) by the maximum current durring LSV polarization (usually the starting current). Electrodes made from commercially purchased magnetite, magnetically separated magnetite, maghemite, and the agarose control all had iR drops that were less than 1 mV. The iron electrodes had iR drops of 1 to 9 mV. Electrodes made from the magnetite synthesized by collaborators had iR drops that were always less than 5 mV with 3 exceptions: an $x = 0.45$, $x = 0.49$, and $x = 0.39$ had iR drops of 18, 21, and 25 mV, respectively.

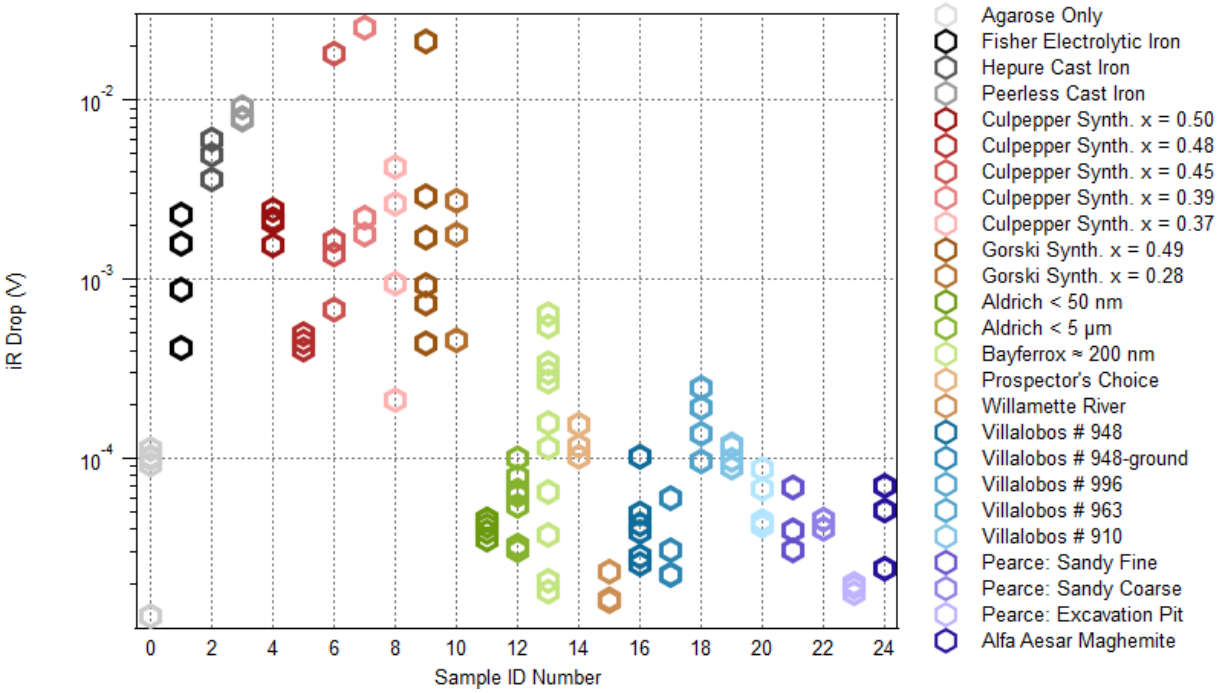

Figure 22. iR drop calculated from solution resistance determined by EIS multiplied by the maximum current observed during LSV.

Method Development: Agarose Binder. Preliminary electrode preparations used GenePure LE agarose from BioExpress, but we switched to an agarose with a lower melting temperature (Fisher BP1360) to avoid exposing the samples to temperatures greater than 50 ºC. Dry agarose and sample powder (by weight, the agarose to sample ratio was 1:100) were mixed with the electrolyte, brought to a boil on a hot plate, and allowed to cool on the benchtop. This slurry was reheated on a hot plate, vortexed for 1 minute to suspend sample, and pipetted into the well of the PDE. In an effort to minimize the amount of agarose used in the electrode, early experiments used 0.25 to 1.0 wt% agarose in electrolyte. After multiple electrode failures, the agarose concentration was raised to 1.5 wt%, and finally to 2.0 wt% in order to stabilize heavier, more granular powders. Agarose gel was prepared with the same electrolyte used in the cell (0.1875 M borate buffer at pH 8.4) to ensure equilibration. The final protocol for suspending the sample in gel was to make large batches of gel in advance for consistency and then adding a few drops of the gel to about 200 mg of sample powder in a microcentrifuge tube. This slurry was vortexed and used within 48 hours.

Method Development: Packing the Electrode. Preliminary experiments used electrodes made by pipetting the sample slurry into the well of the PDE, then letting the electrode rest on the benchtop for approximately 10 minutes to allow the agarose to solidify. We used impedance spectroscopy (not shown) to compare electrodes and found negligible differences between disks made using this method and disks of agarose alone, so a new protocol for "packing" the electrode by centrifugation was established. The agarose gel-stabilized PDE was packed by centrifugation using two different methods: (*i*) An extension made of shrink-wrap tubing was added to the disk cavity, allowing it to be overfilled with the sample slurry prior to centrifugation for 15 minutes at 3200 rpm, after which the extension was removed and the excess material was cut away, leaving the packed material surface flush with the Teflon sheath (**Figure 2C**). A drop of agarose was added to this surface and the electrode was centrifuged again to smooth this interface with the electrolyte. (*ii*) The disk cavity was filled without an extension; the packed material after centrifuging did not reach the surface of the Teflon sheath. The empty space was filled with agarose gel and the electrode was centrifuged again (**Figure 2D**). We found that the second method gave less noisy impedance spectroscopy data (not included in this study), presumably due to rotation of a smoother surface.

Specific Surface Area (SSA) of most samples was measured by BET N_2 gas adsorption, with a Micromeritics Gemini V Surface Area and Pore Size Analyzer, using the protocol developed in a previous study with iron oxides[2]. The results are included in **Table 1**.

Surface Area Normalization. Electrochemical current and resistance data are usually reported as normalized to surface area, i.e. $A \cdot cm^{-2}$ or $\Omega \cdot cm^2$. The surface area used for this calculation is usually the geometric area of the exposed disk surface.[3-6] Because we are working with packed powder electrodes, it is clear that the exposed surface area could be greater than the geometric surface area of the packed-particle/electrolyte interface. A mass-based surface area was calculated by retrieving and drying the packed disk after characterization (**Figure 2E**), weighing the dried disk to get total mass (the mass from residual agarose is insignificant), and multiplying by the SSA (by BET on unused material) to obtain the total surface area of particles contained in the disk. This calculation assumes that the entire particle surface is exposed to electrolyte and electroactive, which should be an over estimate because some of the surface area will obstructed by contact between particles and between the particles and the confining walls of the electrode well. The expectation was that by using this normalization method, we would see replicate values consolidate and we would see greater separation between samples, and this approximation was expected to be more appropriate for our PDE than the external, geometric surface area used with conventional disk electrodes.

All data was normalized and compared using both methods, an example of which is shown in **Figure 23**. The calculated mass-based surface area was tens to ten thousands of cm^2, while the geometric surface area of the electrode was 0.196 cm^2. Normalizing by the mass-based surface area resulted in unrealistically low current (and high resistance) values. Hence, the surface area normalized current data in **Figure 23A show** the agarose (grey) electrode gives far greater current because it can only be normalized by geometric surface area, the iron electrode (black) appears to have a significantly stronger current signal than the synthesized magnetite electrode (red), and the commercial (green) and magnetically separated (blue) magnetite have similar current values although there is clearly more noise in the commercial signal. In contrast, the surface area normalized current data in **Figure 23B** shows that the current signal for the agarose, synthesized magnetite, and iron samples were comparable. Noise increases with decreased signal strength, apparent in the low-current portions of both figures. Based on these

data, we chose to use the geometric normalization instead for two reasons: (*i*) the SSA value for a sample was often far greater than the value being measured, so error in the surface area estimate could obscure smaller differnces in the measured current, and (*ii*) using the geometric surface area resulted in values that were comparable to other published data for similar (non-powder) material.[7]

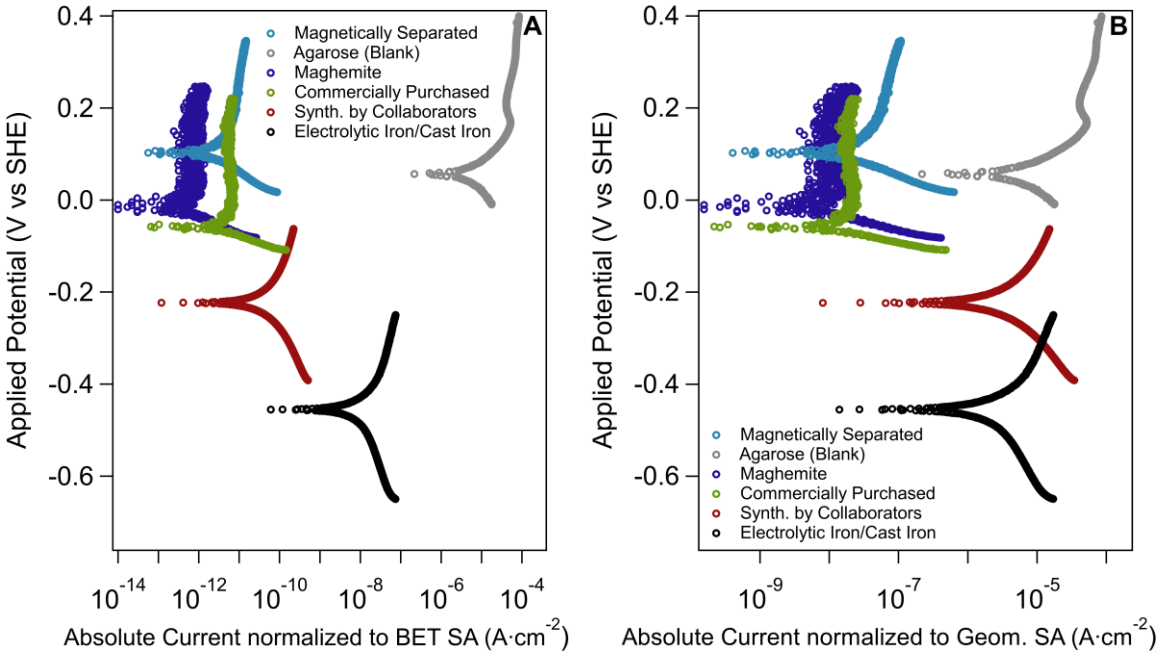

Figure 23. Comparison of applied potential vs resulting current normalized by two different measures of surface area. (A) Current normalized to the mass-based surface area of the packed disk. (B) Current normalized to the geometric surface area of the exposed disk.

References in Appendix A

1. Mansfeld, F., The effect of uncompensated IR-drop on polarization resistance measurements. *Corrosion* **1976,** *32*, (4), 143-146.

2. Fan, D.; Bradley, M.; Hinkle, A. W.; Johnson, R. L.; Tratnyek, P. G., Chemical reactivity probes for assessing abiotic natural attenuation by reducing iron minerals. *Environ. Sci. Technol.* **2016,** *50*, (4), 1868-1876; DOI: 10.1021/acs.est.5b05800.

3. Albertus, F.; Llerena, A.; Alpızar, J.; Cerdá, V.; Luque, M.; Rıos, A.; Valcárcel, M., A PVC–graphite composite electrode for electroanalytical use. Preparation and some applications. *Anal. Chim. Acta* **1997,** *355*, (1), 23-32.

4. Hamadou, L.; Kadri, A.; Benbrahim, N., Characterisation of passive films formed on low carbon steel in borate buffer solution (pH 9.2) by electrochemical impedance spectroscopy. *Appl. Surf. Sci.* **2005,** *252*, (5), 1510-1519.

5. Zhu, H.; Zhang, Y.; Yue, L.; Li, W.; Li, G.; Shu, D.; Chen, H., Graphite–carbon nanotube composite electrodes for all vanadium redox flow battery. *J. Power Sources* **2008,** *184*, (2), 637-640.

6. Rodriguez-Lopez, A.; Torres-Torres, D.; Mojica-Gomez, J.; Estrada-Arteaga, C.; Antano-Lopez, R., Characterization by electrochemical impedance spectroscopy of magnetite nanoparticles supported on carbon paste electrode. *Electrochim. Acta* **2011,** *56*, (23), 8078-8084; DOI: 10.1016/j.electacta.2010.11.039.

7. White, A. F.; Peterson, M. L.; Hochella, M. F., Jr., Electrochemistry and dissolution kinetics of magnetite and ilmenite. *Geochim. Cosmochim. Acta* **1994,** *58*, (8), 1859-75; DOI: 10.1016/0016-7037(94)90420-0.

8. Nurmi, J. T.; Bandstra, J. Z.; Tratnyek, P. G., Packed powder electrodes for characterizing the reactivity of granular iron in borate solutions. *J. Electrochem. Soc.* **2004,** *151*, (6), B347-B353.

9. Nurmi, J. T.; Tratnyek, P. G.; Sarathy, V.; Baer, D. R.; Amonette, J. E.; Pecher, K.; Wang, C.; Linehan, J. C.; Matson, D. W.; Penn, R. L.; Driessen, M. D., Characterization and properties of metallic iron nanoparticles: Spectroscopy, electrochemistry, and kinetics. *Environ. Sci. Technol.* **2005,** *39*, (5), 1221-1230; DOI: 10.1021/es049190u.

10. Nurmi, J. T.; Tratnyek, P. G., Electrochemical studies of packed iron powder electrodes: Effects of common constituents of natural waters on corrosion potential. *Corros. Sci.* **2008,** *50*, (1), 144-154; DOI: 10.1016/j.corsci.2007.06.016

11. Culpepper, J.; Scherer, M.; Robinson, T.; Neumann, A.; Cwiertny, D.; Latta, D., Reduction of PCE and TCE by magnetite revisited. *Environ. Sci. Proc. Impacts* **2018,** *20*, (10), 1340-1349 DOI: 10.1039/c8em00286j.

12. Gorski, C. A.; Nurmi, J. T.; Tratnyek, P. G.; Hofstetter, T. B.; Scherer, M. M., Redox behavior of magnetite: Implications for contaminant reduction. *Environ. Sci. Technol.* **2010,** *44*, (1), 55-60; DOI: 10.1021/es9016848.

13. Salazar-Camacho, C.; Villalobos, M.; Rivas-Sánchez, M. d. l. L.; Arenas-Alatorre, J.; Alcaraz-Cienfuegos, J.; Gutiérrez-Ruiz, M. E., Characterization and surface reactivity of natural and synthetic magnetites. *Chem. Geol.* **2013,** *347*, (0), 233-245; DOI: 10.1016/j.chemgeo.2013.03.017.

14. Villacís-García, M.; Villalobos, M.; Gutiérrez-Ruiz, M., Optimizing the use of natural and synthetic magnetites with very small amounts of coarse Fe(0) particles for reduction of aqueous Cr(VI). *J. Hazard. Mater.* **2015,** *281*, 77-86.

15. Pearce, C. I.; Liu, J.; Baer, D. R.; Qafoku, O.; Heald, S. M.; Arenholz, E.; Grosz, A. E.; McKinley, J. P.; Resch, C. T.; Bowden, M. E.; Engelhard, M. H.; Rosso, K. M., Characterization of natural titanomagnetites ($Fe_{3-x}Ti_xO_4$) for studying heterogeneous electron transfer to Tc(VII) in the Hanford subsurface. *Geochim. Cosmochim. Acta* **2014,** *128*, (0), 114-127; DOI: 10.1016/j.gca.2013.12.010.

16. Langmuir, D., *Aqueous Environmental Geochemistry*. Prentice-Hall, Inc.: Upper Saddle River, NJ, 1997; p 600merlrefs.

17. Rickard, D.; Luther, G. W., Chemistry of iron sulfides. *Chem. Rev.* **2007,** *107*, (2), 514-562; DOI: 10.1021/cr0503658.

18. Stumm, W.; Morgan, J. J., *Aquatic Chemistry: Chemical Equilibria and Rates in Natural Waters*. 3rd ed.; Wiley: New York, 1996; p 1022.

Appendix B: Summary of Magnetite Sample Properties

Table 1. Summary of magnetite sample properties

Name	ID No.	Material Category	Supplier	Supplier ID, Date Received	Description	Sieve + Particle Size	SSA[1] (m^2/g)	Refs
FisherFePowder	1	Electrolytic iron	Fisher Scientific (Pittsburgh, PA)	I-60 4/2006	Electrolytic Powder, >99% Fe	>100 mesh, 0.2 μm	0.083	8-10
HepureCastFe	2	Cast iron	Hepure (Flemington, NJ)	HCA-150 7/2011	Cast Iron Powder	Powder	1.5	
PeerlessCastFe	3	Cast iron	Peerless (Detroit, MI)	50D UDC 8/2011	Cast Iron Powder	Powder	1.9	
JCX050Mag	4	Magnetite synthesized by collaborators	J. Culpepper, M. Scherer Lab, University of Iowa	4/2016	x = 0.50 (Labelled stoichiometry)	Powder	65[2]	11
JCX048Mag	5	Magnetite synthesized by collaborators	J. Culpepper, M. Scherer Lab, University of Iowa	4/2016	x = 0.48 (Labelled stoichiometry)	Powder	70[2]	11
JCX045Mag	6	Magnetite synthesized by collaborators	J. Culpepper, M. Scherer Lab, University of Iowa	4/2016	x = 0.45 (Labelled stoichiometry)	Powder	~70[2]	11
JCX039Mag	7	Magnetite synthesized by collaborators	J. Culpepper, M. Scherer Lab, University of Iowa	4/2016	x = 0.39 (Labelled stoichiometry)	Powder	~70[2]	11
JCX037Mag	8	Magnetite synthesized by collaborators	J. Culpepper, M. Scherer Lab, University of Iowa	4/2016	x = 0.37 (Labelled stoichiometry)	Powder	75[2]	11

StoiX049Mag	9	Magnetite synthesized by collaborators	C. Gorski, M. Scherer Lab, University of Iowa	1/2010	x = 0.49 (Labelled stoichiometry)	Powder	86[2]	12
StoiX028Mag	10	Magnetite synthesized by collaborators	C. Gorski, M. Scherer Lab, University of Iowa	1/2010	x = 0.28 (Labelled stoichiometry)	Powder	66[2]	12
Ald50nMag	11	Commercially purchased magnetite	Aldrich (St. Louis, MO)	637106 4/2014	Magnetite powder, 97%	50-100 nm	9.0	13, 14
Ald5uMag	12	Commercially purchased magnetite	Aldrich (St. Louis, MO)	310069 4/2014	Magnetite powder, 95%	<5 μm	6.8	13, 14
BayMag	13	Commercially purchased magnetite	Bayferrox (Burgettstown, PA)	318NM 3/2014	Magnetite powder, 97%	0.2 μm	12	
MagnetiteSand	14	Magnetically separated magnetite	Prospector's Choice, (Surprise, AZ)	5/2015	Magnetite black sand	20 mesh	1.8	
WKPP075Mag	15a	Magnetically separated magnetite	Sediment from Willamette River, Portland, OR	7/2017	Collected at Kelley Point Park, Portland	75-147 μm	1.9	
WKPP147Mag	15b	Magnetically separated magnetite	Sediment from Willamette River, Portland, OR	7/2017	Collected at Kelley Point Park, Portland	147-175 μm	2.0	
Vill3Mag	16	Magnetically separated magnetite	Mario Villalobos, Pena Colorada iron ore mine, Mexico	2/2016	Sample 948	48 nm[3]	3.0[3]	13, 14
Vill4Mag	17	Magnetically separated magnetite	Mario Villalobos, Pena Colorada iron ore mine, Mexico	2/2016	Sample 948-fine	39 nm[3]	7.6[3]	13, 14
Vill5Mag	18	Magnetically separated magnetite	Mario Villalobos, Pena Colorada iron ore mine, Mexico	2/2016	Sample 996	52 nm[3]	1.4[3]	13, 14
Vill6Mag	19	Magnetically separated magnetite	Mario Villalobos, Pena Colorada iron ore mine, Mexico	2/2016	Sample 963	50 nm[3]	2.1[3]	13, 14

Vill7Mag	20	Magnetically separated magnetite	Mario Villalobos, Pena Colorada iron ore mine, Mexico	2/2016	Sample 910	50 nm[3]	1.4[3]	13, 14
CPSFMag	21	Magnetically separated magnetite	Carolyn Pearce, Hanford Formation	9/2016	"Sandy fine" sample from submarine burial site	Fine sand	2.3	15
CPSCMag	22	Magnetically separated magnetite	Carolyn Pearce, Hanford Formation	9/2016	"Sandy coarse" sample from submarine burial site	Coarse sand	~2[4]	15
CPERDFMag	23	Magnetically separated magnetite	Carolyn Pearce, Hanford Formation	9/2016	From Environmental Remediation and Disposal Facility excavation site	Coarse sand	~0.2[4]	15
AAMgh	24	Maghemite	Alfa Aesar, Ward Hill, MA	45007 9/2015	NanoArc synthesized	20-40 nm	37	

Table 2. Summary of magnetite characterization results.

Name	ID No.	E_{OC} (V vs SHE)	$E_{0,LPR}$ (V vs SHE)	$E_{0,LSV}$ (V vs SHE)	$R_{P,LPR}$ (kΩ·cm^2)	$R_{P,R}$ (kΩ·cm^2)	i_{CALC} (nA·cm^{-2})	Fe(II)/Fe(III) (fraction, x)
Agarose	0	0.049±0.011	0.068±0.010	0.072±0.015	403±133	531±250	45.7±12.3	N/A
FisherIron	1	−0.475±0.025	-0.475±0.026	−0.486±0.037	9.19±2.93	15.0±4.33	843±703	N/A
HepureCastIron	2	−0.385±0.127	-0.387±0.127	−0.387±0.129	2.10±2.28	5.15±5.37	7630±10300	N/A
PeerlessCastIron	3	−0.453±0.004	-0.456±0.004	−0.465±0.004	0.319±0.117	0.933±0.218	13700±4420	N/A
JCX050Mag	4	−0.195±0.011	-0.196±0.011	−0.229±0.012	6.31±1.28	8.26±1.59	4220±1310	0.41±0.03
JCX048Mag	5	−0.054±0.092	-0.055±0.093	−0.114±0.069	105±56.7	153±81.2	406±48.6	0.46±0.05[2]
JCX045Mag	6	−0.242±0.018	-0.243±0.018	−0.263±0.018	10.6±8.28	12.4±9.55	6870±10700	N/A
JCX039Mag	7	−0.220±0.007	-0.221±0.007	−0.249±0.009	0.601±0.359	0.771±0.386	42400±16300	0.41±0.03[2]
JCX037Mag	8	−0.090±0.057	-0.090±0.059	−0.124±0.053	27.0±30.5	37.1±43.8	2750±2600	0.32±0.02[2]
StoiX049Mag	9	−0.038±0.126	-0.043±0.123	−0.127±0.091	19.9±21.9	34.9±41.9	12600±16600	N/A
StoiX028Mag	10	0.004±0.134	0.000±0.132	−0.072±0.092	15.3±8.11	24.2±19.5	3810±1880	0.21±0.02[2]
Ald50nMag	11	0.204±0.013	0.204±0.015	0.129±0.008	681±127	1330±408	60.2±17.1	0.27±0.01[2]
Ald5uMag	12	0.083±0.089	0.082±0.089	−0.033±0.078	668±523	710±170	174±70.2	0.23±0.01[2]
BayMag	13	0.181±0.060	0.180±0.059	0.072±0.089	584±440	760±1040	902±1310	0.34±0.02
MagnetiteSand	14	0.012±0.020	0.018±0.021	−0.072±0.012	567±216	926±211	92.1±14.0	0.39±0.04
WKPP075Mag[2]	15a	0.175±0.008	0.182±0.014	−0.010±0.008	2510±1400	134±31.8	1420±332	0.64±N/A[3]
WKPP147Mag[2]	15b	0.163±0.032	0.180±0.028	−0.023±0.036	2920±295	186±111	1230±762	0.65±0.05[2]
Vill3Mag	16	0.195±0.036	0.197±0.037	0.090±0.048	482±156	1380±549	91.6±49.4	0.48±0.01
Vill4Mag	17	0.234±0.013	0.231±0.013	0.113±0.011	392±214	1120±756	173±132	0.46±0.02
Vill5Mag	18	0.240±0.011	0.237±0.011	0.132±0.019	315±204	551±336	239±104	0.50±0.01
Vill6Mag	19	0.225±0.014	0.223±0.015	0.126±0.026	368±85.8	772±162	131±17.9	0.51±0.02
Vill7Mag	20	0.219±0.015	0.221±0.013	0.102±0.030	867±489	1750±624	73.7±29.7	0.51±0.01
CPSFMag	21	0.181±0.031	0.182±0.026	0.054±0.042	686±331	1540±670	93.4±36.9	0.39±0.04
CPSCMag[2]	22	0.228±0.027	0.224±0.025	0.125±0.014	573±160	1070±287	101±39.4	0.40±0.02
CPERDFMag	23	0.204±0.026	0.207±0.027	0.071±0.011	1490±677	2210±660	65.0±25.0	0.42±0.04
AAMgh	24	0.162±0.040	0.160±0.034	0.050±0.066	624±511	1310±692	114±81.0	N/A

Table 3. Summary of EIS analysis characterization.[1]

Name	ID No.	R_S ($\Omega \cdot cm^2$)	CPE_1 (at 1 kHz) ($\Omega \cdot cm^2$)	R_P ($k\Omega \cdot cm^2$)	CPE_2 (at 1 kHz) ($\Omega \cdot cm^2$)
Agarose	0	73.7±13.7	11.2±4.1	555.2±280.3	410.3±308.1
FisherIron	1	53.9±7.6	30.8±8.4	9.3±3.4	13.4±11.1
HepureCastIron	2	22.6±8.5	26.7±13.9	2.6±3.0	16.9±22.3
PeerlessCastIron	3	24.9±3.9	26.1±5.7	0.1±0.1	0.7±0.4
JCX050Mag	4	67.7±3.0	10.5±3.3	5.6±1.4	13.8±9.1
JCX048Mag	5	66.4±8.0	22.0±0.5	126.6±177.7	18.7±17.2
JCX045Mag	6	53.2±4.3	14.7±4.2	8.5±8.3	38.2±37.4
JCX039Mag	7	53.0±15.7	12.9±1.2	0.5±0.3	2.0±0.9
JCX037Mag	8	59.5±14.1	19.0±7.0	21.3±25.5	145.3±182.0
StoiX049Mag	9	43.6±5.7	27.4±19.4	0.5±0.2	14.0±11.3
StoiX028Mag	10	56.4±4.7	14.7±4.5	1.9±2.3	55.1±59.7
Ald50nMag	11	73.0±15.0	31.5±8.4	514.1±395.1	3.8e3±2.7e3
Ald5uMag	12	57.0±10.1	25.3±12.8	147.8±113.4	1.8e3±3.3e3
BayMag	13	70.6±19.4	20.0±4.5	351.0±700.0	3.1e3±6.2e3
MagnetiteSand	14	74.5±18.5	61.3±8.9	0.1±0.1	18.4±1.1
WKPP075Mag[2]	15a	93e3±8e3	266e3±52e3	113.2±13.8	47.4e3±7.7e3
WKPP147Mag[2]	15b	94e3±50e3	161e3±121e3	55.1±45.5	28.5e3±13.1e3
Vill3Mag	16	125.0±12.4	79.1±45.8	109.4±200.0	74.1±111.5
Vill4Mag	17	87.5±8.2	24.5±3.4	18.4±14.0	243.0±75.9
Vill5Mag	18	139.8±8.2	61.0±26.6	41.2±82.3	38.2±25.5
Vill6Mag	19	112.9±5.6	305.6±450.6	51.4±102.7	20.5±1.4
Vill7Mag	20	126.6±1.8	114.7±10.9	0.1±0.0	23.1±3.1
CPSFMag	21	91.8±18.2	111.1±37.1	75.5±130.8	243.3±352.2
CPSCMag[2]	22	67.8±7.8	78.9±53.0	103.2	509.7±536.6
CPERDFMag	23	52.7±3.7	89.5±21.0	0.1±0.0	49.8±1.8
AAMgh	24	75.7±32.9	23.4±1.0	117.0±37.1	583.4±418.2

[1] Values are averages ± 1 standard deviation from 3 or more replicates unless otherwise noted.

[2] n = 2.

Table 4. Summary of magnetite characterization Tafel fitting results.[1]

Name	ID No.	β_c (V/decade)	β_a (V/decade)	$R_{P,T}$ (kΩ·cm^2)	i_{COR} (Tafel) (nA·cm^{-2})
Agarose	0	0.195±0.078	0.316±0.079	533±221	103±38.1
FisherIron	1	0.459±0.352	0.183±0.128	15.6±3.79	3590±2350
HepureCastIron	2	0.092±0.058	0.087±0.021	5.12±5.42	8070±8560
PeerlessCastIron	3	0.060±0.015	0.066±0.019	0.993±0.252	14300±4770
JCX050Mag	4	0.654±0.183	0.303±0.025	8.37±1.53	11200±4080
JCX048Mag	5	0.258±0.122	0.136±0.101	171±92.9	403±515
JCX045Mag	6	0.480±0.105	0.348±0.070	12.9±10.0	37500±64100
JCX039Mag	7	0.653±0.051	0.344±0.070	0.785±0.403	146000±63600
JCX037Mag	8	0.547±0.127	0.245±0.034	38.4±45.9	6900±6790
StoiX049Mag	9	0.486±.0202	0.168±0.178	33.9±41.3	36200±82200
StoiX028Mag	10	0.437±0.172	0.134±0.045	24.0±19.2	3030±2310
Ald50nMag	11	0.459±0.241	0.108±0.031	1210±295	34.4±20.5
Ald5uMag	12	0.126±0.080	0.253±0.240	744±227	34.1±21.5
BayMag	13	0.313±0.271	0.123±0.131	742±987	101±76.7
MagnetiteSand	14	0.074±0.008	0.594±0.025	922±222	32.5±10.8
WKPP075Mag[2]	15a	0.086±0.008	0.022±0.000	128±30.6	61.5±13.8
WKPP147Mag[2]	15b	0.087±0.071	0.022±0.011	172±88.7	42.6±3.75
Vill3Mag	16	0.468±0.239	0.095±0.021	1080±353	34.9±17.6
Vill4Mag	17	0.344±0.079	0.079±0.010	938±597	45.6±35.8
Vill5Mag	18	0.585±0.174	0.095±0.029	615±458	83.6±47.4
Vill6Mag	19	0.396±0.275	0.094±0.030	707±85.9	45.4±20.0
Vill7Mag	20	0.392±0.021	0.059±0.022	1950±750	14.1±11.3
CPSFMag	21	0.292±0.105	0.054±0.016	1400±585	15.6±8.25
CPSCMag[2]	22	0.529±0.081	0.084±0.004	1030±290	31.6±6.95
CPERDFMag	23	0.387±0.108	0.051±0.008	3970±1910	5.57±2.21
AAMgh	24	0.363±0.123	0.169±0.187	1470±855	50.6±67.9

[1] Values are ± 1 standard deviation from 3 or more replicates unless otherwise noted.

[2] n = 2.

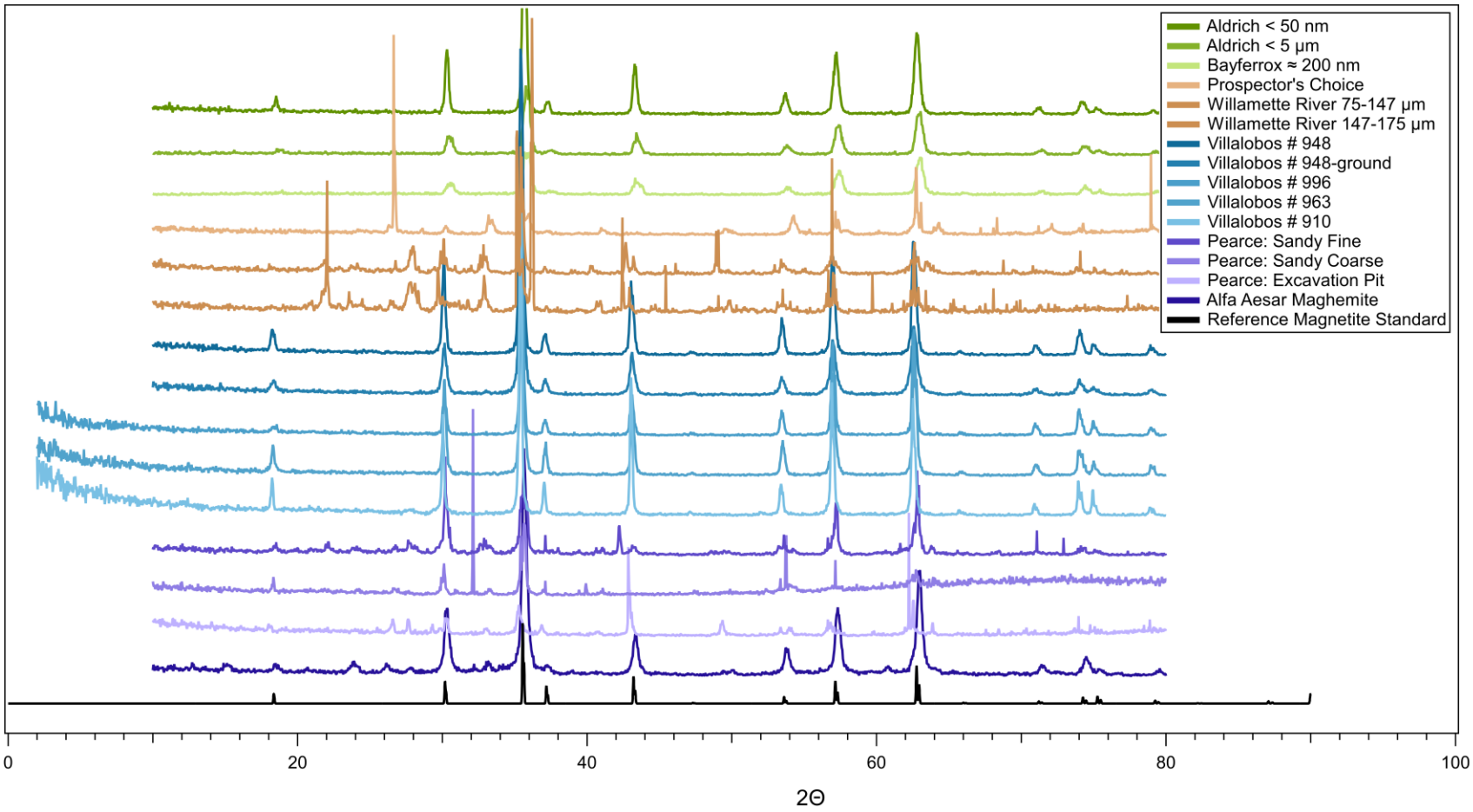

Figure 24. XRD Spectra overlay with magnetite reference standard. X-ray diffraction (XRD) analysis was performed using a Rigaku MiniFlex600 X-ray diffractometer with 40 kW/15 mA radiation (Willamette river samples used 40 kW/44 mA radiation). Diffraction patterns were collected over a range of 10 to 80º of 2Θ, using a step size of 0.04º and time per step of 0.5 s.

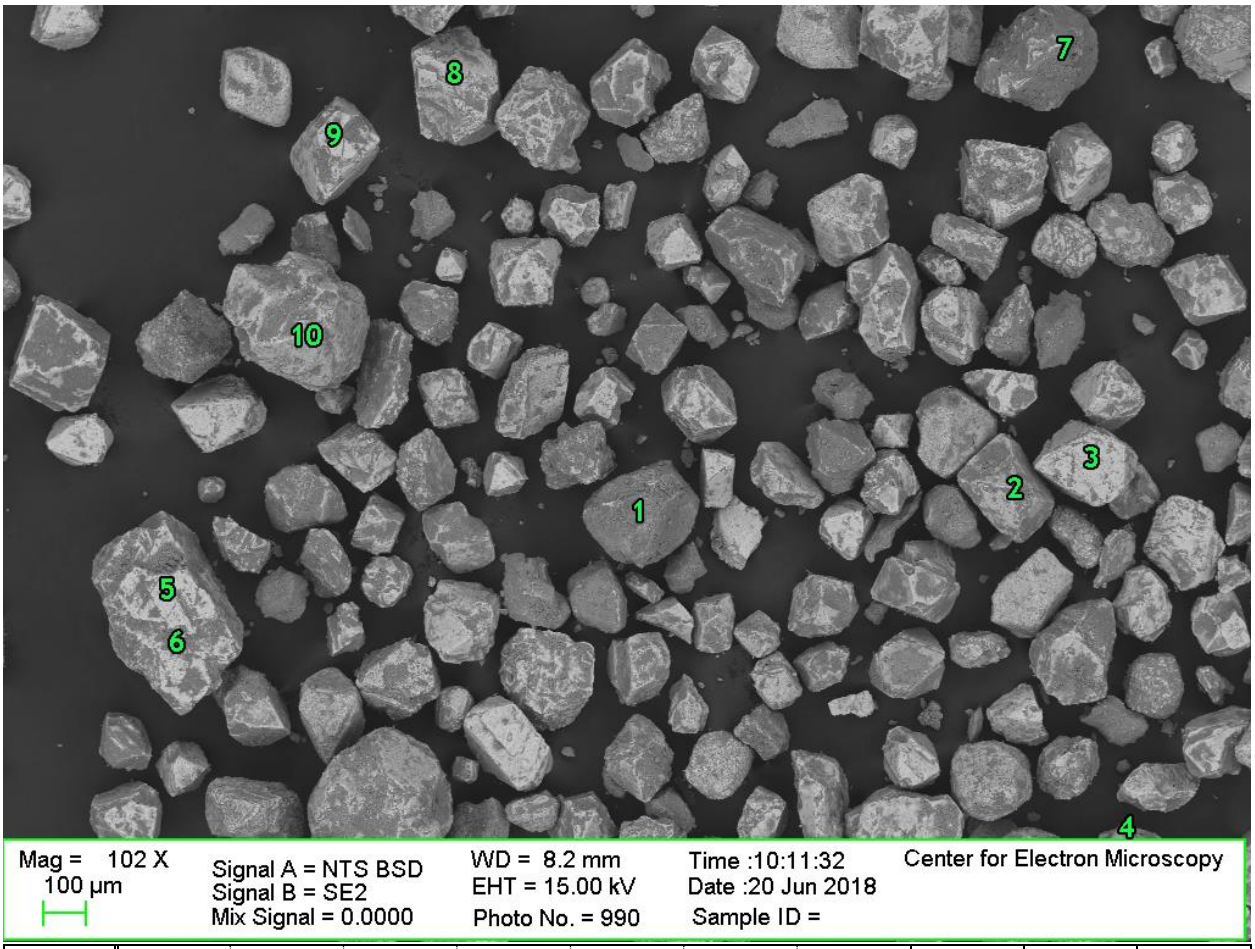

	1	2	3	4	5	6	7	8	9	10
Fe	44.6	25.4	82.2	54.4	74.7	9.8	18.9	74.7	75.4	81.2
O	24.6	36.2	15.9	29.3	22.2	43.7	28.7	19.4	20.5	8.5
Si	14.5	22.3	0.9	8.9	1.6	22.9	25.7	2.8	1.9	3.2
Al	12.2	14.4	0.7	5.7	1.3	16.4	14.3	2.4	1.8	2.3
Ti	0.4		0.2			0.6	0.4	0.2	0.2	3.0
Mg	2.0	0.7		0.9		4.0	5.3	0.2		0.4
K	1.8	0.3		0.6		1.4	6.0			1.1
Ca		0.8		0.2		1.2	0.6			0.2
V					0.2			0.2	0.3	0.3
P								0.2		

Figure 25. SEM-EDS Characterization of Prospector's Choice Sample.

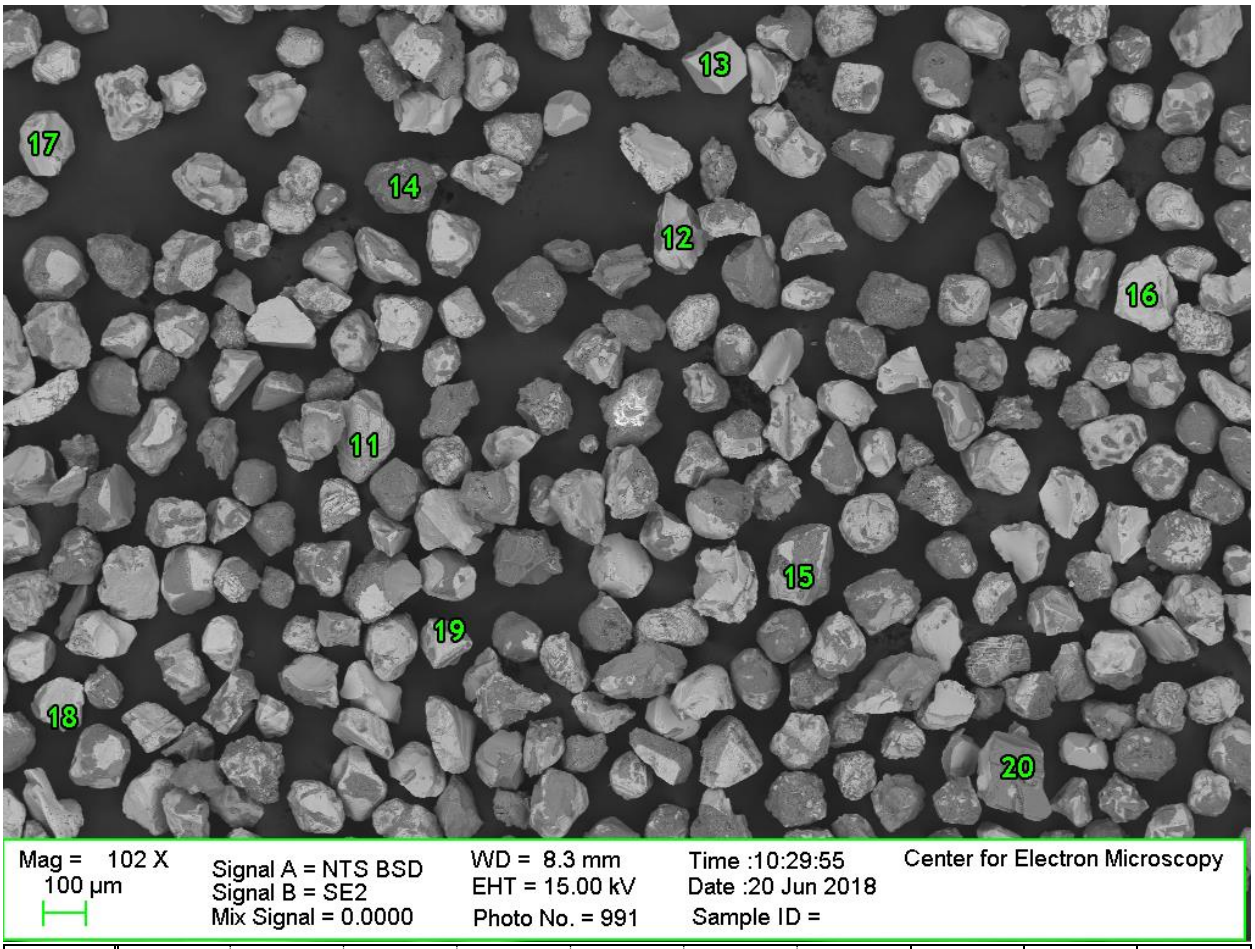

	11	12	13	14	15	16	17	18	17	20
Fe	28.9	39.3	47.0	1.3	39.5	70.1	80.7	71.7	57.2	12.8
O	28.4	37.3	26.1	52.4	33.2	17.0	12.5	16.5	18.4	33.6
Si	2.3	0.8	0.2	35.0	6.6	0.7	0.7	1.5	3.3	25.5
Al	1.2	0.6	0.4	5.7	3.4	1.0	0.6	1.6	1.9	5.4
Ti	32.1	20.3	24.6	0.3	9.9	9.2	4.6	6.6	12.2	2.0
Mg	0.5	1.8	1.8		2.0	0.6	0.2	0.9	1.8	8.8
K				2.9					0.5	0.5
Ca	1.2				2.3	0.4			0.9	10.2
V	0.4				0.4	0.5	0.4	0.5	0.6	
P	0.2				1.1		0.1		0.3	
Na				2.4						1.2
Mn	1.0				1.1	0.5	0.3	0.4	1.6	
Pb	0.8									
Zn	3.1								1.2	
Cr					0.6					
In								0.3		

Figure 26. SEM-EDS Characterization of Willamette River 75-147 µm sample.

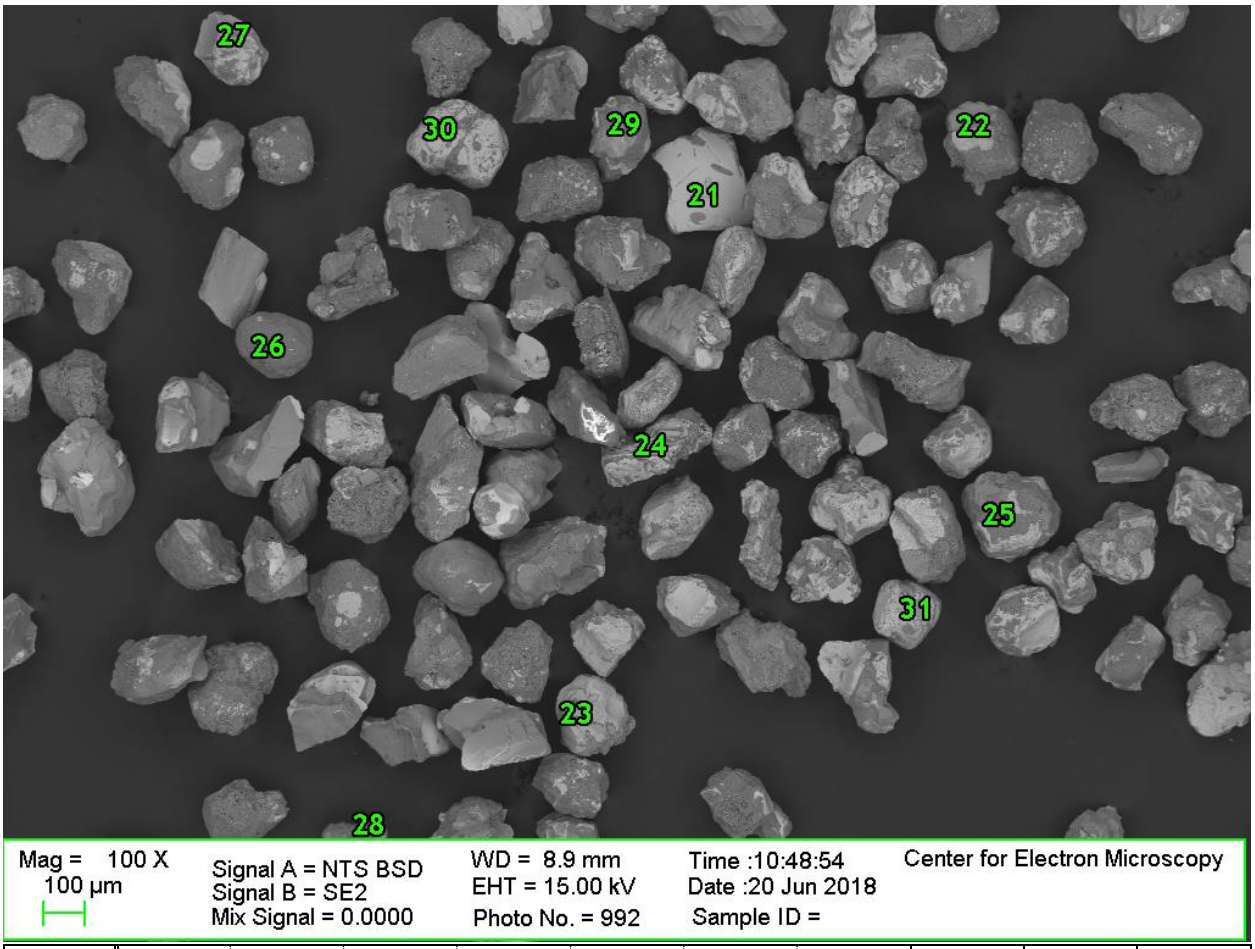

	21	22	23	24	25	26	27	28	29	30
Fe	48.1	37.1	37.7	23.8	62.4	2.0	43.6	0.7	0.9	39.0
O	25.1	37.8	34.2	35.9	16.5	44.2	35.1	45.7	44.8	32.4
Si	0.3	0.4	0.3	21.1	1.5	6.4	1.8		16.3	0.7
Al	0.3	0.4	0.2	6.1	2.0	40.6	1.7	0.3	26.6	0.9
Ti	25.0	22.1	24.7	2.3	14.7	0.3	11.2			24.6
Mg	1.3	2.2	2.6	6.6	0.8		1.3	0.2		1.9
K				0.2		3.6			0.2	
Ca				0.5	0.4	0.4	0.7	32.4	7.5	0.1
V				0.3	0.7		0.3			
P				0.2			0.3	17.3		
Na					0.5	2.5			3.8	
Mn			0.4	1.0	0.5		0.4			0.4
Pb										
Zn				1.8			3.6			
Cr								2.8		
In								0.7		

Figure 27. SEM-EDS Characterization of Willamette River 147-175 µm sample.

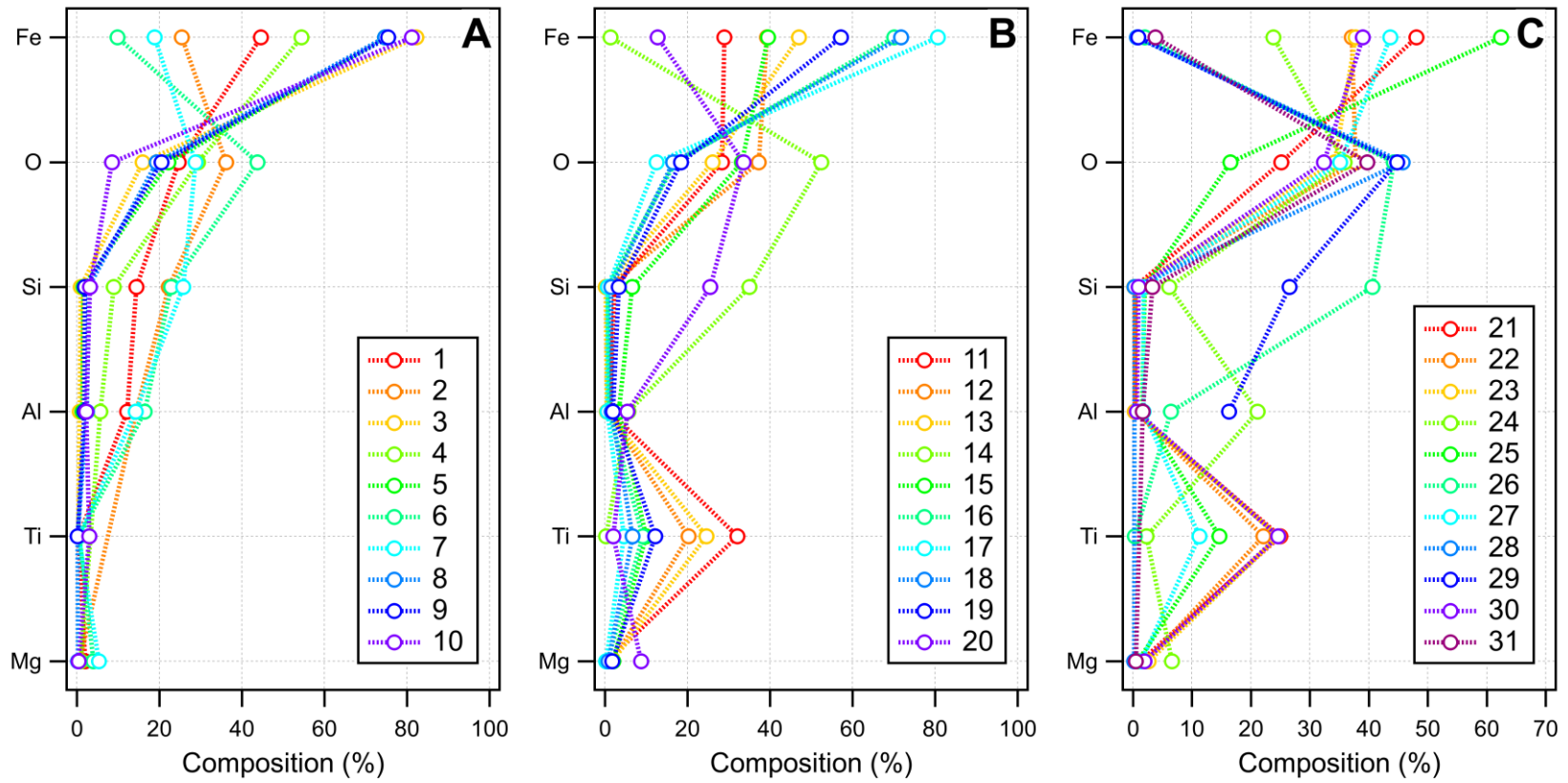

Figure 28. Major components of: (A) Prospector's Choice magnetite sand, (B) Willamette River 75-147 µm size fraction, (C) Willamette River 147-175 µm size fraction, from SEM-EDS analysis. Numbers correspond with the tables in Part B of Figures 25-27.

Table 5. Thermodynamic potentials for half-reactions of relevant iron oxides.

Redox Couple	Half Reaction	ΔG_{rxn} (kJ/mol)[1]	E^0 (V)	E_H (pH 8.4) (V)[2]
Fe_3O_4 / $Fe(OH)_2$	$Fe_3O_4(s) + 2\ H_2O + 2\ H^+ + 2\ e^- \rightarrow 3\ Fe(OH)_2(s)$	30.06	−0.156	−0.652
Fe^{2+} / Fe^0	$Fe^{2+} + 2\ e^- \rightarrow Fe^0$	78.87	−0.409	−0.631
Fe_3O_4 / FeO	$Fe_3O_4(s) + 2\ H^+ + 2\ e^- \rightarrow 3\ FeO(s) + H_2O$	25.02	−0.130	−0.626
Fe_3O_4 / Fe^0	$Fe_3O_4(s) + 8\ H^+ + 8\ e^- \rightarrow 3\ Fe^0(s) + 4\ H_2O$	66.78	−0.087	−0.583
FeO / Fe^0	$FeO(s) + 2\ H^+ + 2\ e^- \rightarrow Fe^0(s) + H_2O$	13.92	−0.072	−0.569
α−Fe_2O_3 / Fe_3O_4	$3\ \alpha{-}Fe_2O_3(s) + 2\ H^+ + 2\ e^- \rightarrow 2\ Fe_3O_4(s) + H_2O$	−1.68	0.009	−0.488
$Fe_3O_4(s)$ / Fe^{2+}	$Fe_3O_4(s) + 8\ H^+ + 2\ e^- \rightarrow Fe^{2+} + 4\ H_2O$	−169.83	0.880	−0.439
α−FeOOH / Fe_3O_4	$3\ \alpha{-}FeOOH(s) + H^+ + e^- \rightarrow Fe_3O_4 + 2\ H_2O$	−24.06	0.249	−0.247
$Fe(OH)_3(s)$ / Fe^{2+}	$Fe(OH)_3(s) + 3\ H^+ + e^- \rightarrow Fe^{2+} + 3\ H_2O$	−102.06	1.058	0.013
γ−$Fe_2O_3(s)$ / Fe_3O_4	$4\ \gamma{-}Fe_2O_3(s) + Fe^{2+} + e^- \rightarrow 3\ Fe_3O_4$	−56.03	0.290	0.068
α−FeOOH / Fe_3O_4	$3\ \alpha{-}FeOOH(s) + e^- \rightarrow Fe_3O_4 + OH^- + H_2O$	55.83	−0.579	0.083
Fe^{3+} / Fe^{2+}	$Fe^{3+} + e^- \rightarrow Fe^{2+}$	−74.27	0.770	0.436
$Fe(OH)_3(s)$ / $Fe_3O_4(s)$	$3\ Fe(OH)_3(s) + H^+ + e^- \rightarrow Fe_3O_4(s) + 5\ H_2O$	−136.34	1.413	0.917

[1] Calculated from ΔG_f obtained from references 16, 17, and 18 in Appendix A.

[2] Calculated using the Nernst equation and given conditions: $[Fe^{2+}(aq)] = 10^{-7}$ M (with activity coefficient of 0.307), $[Fe^{3+}(aq)] = 10^{-12}$ M (with activity coefficient of 0.070) in 0.1875 M borate buffer pH 8.4.